RSC Advances

REVIEW

View Article Online
View Journal | View Issue



CrossMark click for updates

Cite this: *RSC Adv.*, 2014, **4**, 43725

# Antibody nanosensors: a detailed review

E. K. Wujcik,*[a] H. Wei,[b] X. Zhang,[b] J. Guo,[b] X. Yan,[b] N. Sutrave,[a] S. Wei*[c] and Z. Guo*[b]

Received 15th July 2014
Accepted 4th September 2014

DOI: 10.1039/c4ra07119k

www.rsc.org/advances

In this review, the authors will discuss novel and prospective antibody nanosensors for the detection of specific analytes used in a number of fields of analytical chemistry. Biosensors—transducers that incorporate biological molecules for recognition—have been found to be fundamental in a number of chemical, clinical, and environmental analyses. Antibody nanosensors make up a large area of this research, as the antibodies' specific recognition elements make them highly selective and sensitive. These biological molecules can also be tailored to recognize any single analyte or group of analytes, and can be easily functionalized to a number of nanomaterial substrates. Herein, a number of antibody nanosensor transduction methods will be examined, including electrochemical, optical, magnetic, and piezoelectric, among others that fall into multiple categories. This review will show that it is clear that antibody nanosensors—and nanosensors in general—are highly sensitive no matter the transduction method, and that various transduction methods can be suited for a number of different applications.

## 1. Introduction

Almost every field of science and engineering has the need for sensitive detection of specific analytes. The advent of nanotechnology has brought on many new materials with often enhanced chemical and physical properties—highly tunable size and shape-dependent features, unique and tailorable surface chemistries, high specific surface area, large pore volume per unit mass—and, in turn, many opportunities for the advancement of various sensor platforms.[1–8] The unique properties of nanomaterials have been utilized for the fabrication of nanosensors with enhanced specificity and sensitivity. Some nanomaterials that have bettered the development of nanosensors include nanocarbon allotropes (*i.e.* – fullerenes,[9,10] graphene,[11,12]), nanofibers,[13,14] as well as inorganic nanotubes,[15,16] nanoparticles,[17,18] and quantum dots,[19,20] among

[a]*Materials Engineering And Nanosensor (MEAN) Laboratory, Dan F. Smith Department of Chemical Engineering, Lamar University, Beaumont, TX 77710, USA. E-mail: Evan.Wujcik@lamar.edu*

[b]*Integrated Composites Laboratory (ICL), Dan F. Smith Department of Chemical Engineering, Lamar University, Beaumont, TX 77710, USA. E-mail: Zhanhu.Guo@lamar.edu*

[c]*Department of Chemistry and Biochemistry, Lamar University, Beaumont, TX 77710, USA*

*Dr Evan K. Wujcik is currently an Assistant Professor of Chemical Engineering in the Dan F. Smith Department of Chemical Engineering at Lamar University (Beaumont, TX, USA). He obtained his PhD in Chemical and Biomolecular Engineering from The University of Akron (2013) and his MBA (2011), MS in Chemical Engineering (2009), BS in Applied Mathematics (2010), and BS in Chemical Engineering (2008) from The University of Rhode Island. Dr Wujcik directs the Materials Engineering And Nanosensor (MEAN) Laboratory at Lamar University. His research interests include bionanotechnology, nanocomposites, and nanosensor design & development.*

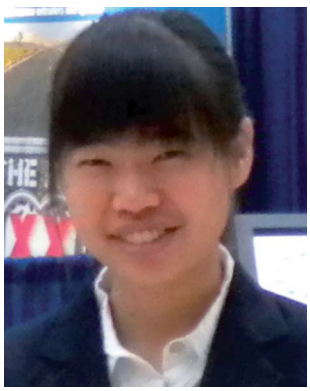

*Ms Huige Wei, currently a PhD candidate in the Dan F. Smith Department of Chemical Engineering at Lamar University, obtained her MS (2011) and BE (2009) degrees from the Department of Chemical Engineering and Technology at Harbin Institute of Technology. Her research interests focus on multifunctional polymer nanocomposites for electrochromic and energy applications.*

many others. Many of these biocompatible nanomaterials have potential in the field of implantable nanosensors and devices.[21–25]

An antibody (Ab)—also known as an immunoglobulin (Ig)—monomer is a globular plasma protein of large molecular weight (~150 kDa).[26] An Ab monomer is made up of four polypeptide chains—two identical light chains (~25 kDa each) and two identical heavy chains (~50 kDa each)—forming its characteristic "Y" shape, as seen in Fig. 1. Each heavy and light chain pair is connected *via* a single disulfide bond. Immunoglobulin in humans exist in five classes—IgA, IgD, IgE, IgG, and IgM—each distinguished by the isotype of their heavy chains. The IgA and IgM occur in dimer and pentamer complexes, respectively, as the IgD, IgE, and IgG occur only as monomers. Isotypes of the small chains also exist in two variations produced on different genes, $\lambda$ and $\kappa$—which can be arranged in many combinations to provide a wide range of antigen recognition.

Each "arm" of the Ab is also made up of two domains, a constant domain and a variable domain. These variable domains dictate the Ab's function and selectivity to specific antigens, or analytes. Within the body, the crystallizable fragment ($F_c$) typically interacts with cell surface receptors or proteins—allowing the immune system to be triggered—while the antigen-binding fragment ($F_{ab}$) interacts with the antigen. The $F_{ab}$ typically has similar function when used in sensors, while the $F_c$ will typically be functionalized to a surface or with a fluorescent tag, magnetic nanoparticle, *etc.* The $F_c$ and $F_{ab}$ of the antibody—containing the carboxyl terminals (–COOH) and amino terminals ($-NH_2$) of the monomer, respectively—are joined by a hinge region, which contributes to the molecule's

*Ms Xi Zhang, currently a PhD candidate in the Dan F. Smith Department of Chemical Engineering at Lamar University, obtained an MS degree from the Department of Mechanical and Automotive Engineering (2010) and a BS degree in Polymer Science and Technology (2006) from South China Institute of Technology. Her research interests include polymer nanocomposites, and conductive nanocomposites.*

*Dr Suying Wei, currently an Assistant Professor in the Department of Chemistry and Biochemistry at Lamar University, obtained a PhD degree in chemistry from Louisiana State University (2006), an MS in applied chemistry from Beijing University of Chemical Technology (2000) and a BS in chemical engineering from Shandong University of Science and Technology (1996). Her research interests include multifunctional composites especially those used in biomedical applications. Her expertise is in analytical, materials and surface chemistry. She was awarded the NSF summer institute fellowship, the Pfizer graduate fellowship, and the Robinson award for excellent research in analytical science during previous appointment.*

*Mr Jiang Guo, currently a PhD candidate in the Dan F. Smith Department of Chemical Engineering at Lamar University, obtained his BE (2012) of Process Equipment and Control Engineering from the School of Chemical and Biological Engineering at Taiyun University of Science and Technology. His research interests include polymer/magnetic nanocomposites.*

*Dr Zhanhu Guo, currently an Associate Professor in Dan F. Smith Department of Chemical Engineering at Lamar University, obtained a PhD degree in Chemical Engineering from Louisiana State University (2005) and received three-year (2005–2008) postdoctoral training in Mechanical and Aerospace Engineering Department at University of California Los Angeles. Dr Guo directs the Integrated Composites Laboratory and chairs the Composite Division of American Institute of Chemical Engineers (AIChE, 2010–2011). His current research focuses on fundamental science behind multifunctional light-weight nanocomposites especially with polymer and carbon as the hosting matrix for electronic devices and environmental remediation applications.*

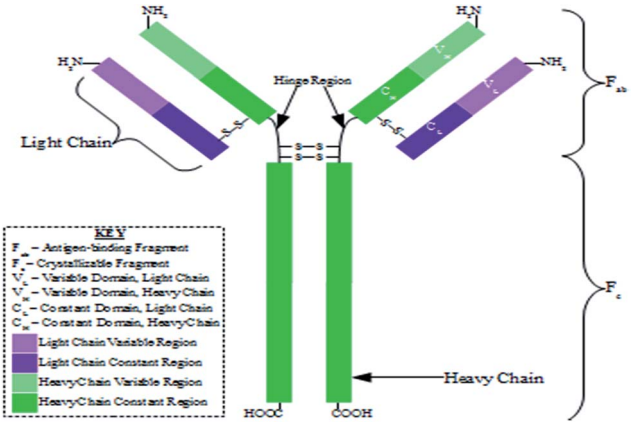


Fig. 1 Schematic showing the structure of the most common antibody (IgG) monomer.

unique biological properties and ability to bind with a high affinity.[27] Here, two disulfide bonds connect the two heavy chains. The short chain and long chain variable regions allow for the selectivity and high affinity binding of specific analytes. Antibodies can be either monoclonal or polyclonal, meaning that they can recognize a single epitope or multiple epitopes, respectively, on a single antigen.

These properties make antibodies attractive for use in a number of fields, but particularly diagnostics.[28] This is mainly due to their biocompatibility with bodily fluids—as well as signaling proteins and antigens—and high affinity binding. Antibodies have been used for many years in the accurate diagnoses of such diseases as cancer,[29,30] rabies,[31] pneumonia,[32] rheumatoid arthritis,[33] Lyme disease,[34] and fungal infections.[35] However, through the development of nanomaterial sensing platforms, the detection limits of these and other novel detection schemes can be lowered.[36,37]

Antibody nanosensors—and nanosensors in general—are made up of a few essential components. At a bare minimum, these sensors require: (1) a means of specific analyte detection (*e.g.* – monoclonal antibody/analyte binding) and (2) a means of transducing this detection into a readable signal (*e.g.* – a measurable change in electrical signal upon the aforementioned monoclonal antibody/analyte binding). Sometimes, an amplification step is also included.[3]

Here, the antibody nanosensors discussed will be classified *via* their transduction method, *i.e.* – electrochemical, optical, magnetic, piezoelectric.[38] All will have a detection scheme requiring the use of an antibody. In this comprehensive review, the authors will discuss novel and prospective antibody nanosensors for the detection of specific analytes from a number of fields with a need for specific detection. Through this, the authors will show that antibody nanosensors—and nanosensors in general—are highly sensitive no matter the transduction method, and that various transduction methods can be suited for a number of different applications.

## 2. Electrochemical antibody nanosensors

An electrochemical (derived from the Greek *elektron* meaning "amber" and the Latin *alchimicus* meaning "of alchemy") technique is a method that deals with the electrical energy and the chemical change occurring at the electrode/electrolyte interface.[39] Compared to other detection technologies such as optical, mechanical, electrical, and magnetic resonance techniques, electrochemical detection is advantageous in that direct data analysis is achieved with the electronic signal output and no further transduction is required, which significantly reduces the complexity of the signal acquisition and the transduction interface—ultimately reducing the cost and increasing the portability of the sensor device.[40–42] Electrochemical antibody nanosensors are based on the conformational changes produced by the biorecognition between the antibody and the antigen, which provides an attractive means for a real time molecular recognition technique that is highly sensitive and selective.[43,44]

Typically, electrochemical antibody nanosensors consist of a working electrode—or sensing electrode—a counter electrode, and a reference electrode.[45] The working electrode serves as the surface where the reaction of interest occurs and the counter electrode is used to make a connection to the electrolyte, allowing current flow between the two electrodes. Usually, both conductive and chemically stable materials including platinum, gold, carbon, and silicon are employed to prepare electrodes.[46] The reference electrode—with a stable and well-defined potential—serves to help apply a desirable potential on the working electrode in a controllable manner. The most commonly used reference electrodes are Ag/AgCl and saturated calomel electrode (SCE).[47]

Typical measurable signals can include current (amperometric), potential (potentiometric), or resistance (impedimetric).[48] Amperometric detection measures the current resulting from the biochemical reactions of electroactive species.[49] For amperometric techniques, the general methods include voltammetry, such as polarography (DC Voltage), linear sweep, differential staircase, normal pulse, reverse pulse, or differential pulse. Cyclic voltammetry (CV) is one of the most widely used, where the voltage is swept between two values at a fixed scan rate. Useful information regarding the redox potential and the electrochemical reaction rates of the analyte reactions can be obtained from CV.[50] Another amperometric technique is chronoamperometry, where a square-wave potential is applied to the working electrode and a steady state current is acquired as a function of time. Chronoamperometry is often used complementary to CV for time-dependent characterization.[51] Potentiometric detection measures the potential at the working electrode referring to the reference electrode in an electrochemical cell with zero or no significant current flowing between them.[52–54] Valuable information regarding the ion activity in an electrochemical reaction can be provided using this technique.

In impedimetric detection, a small sinusoidal potential is applied onto the working electrode and the complex

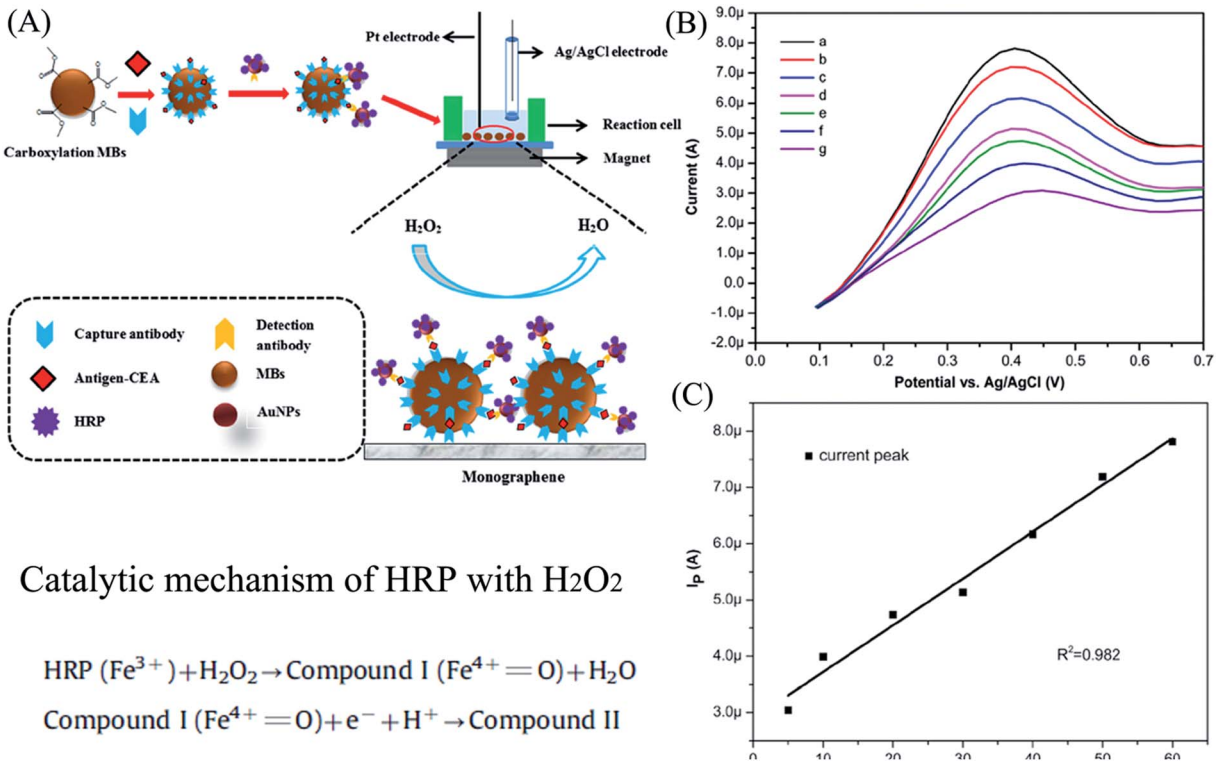


Fig. 2 (A) Preparation of the multi-nanomaterial EC biosensor and CEA detection procedure, (B) CV response of GR/MBs-Ab1/CEA/Ab2-AuNPs-HRP in a sandwich-type immunoassay format for CEA concentrations of (a) 60, (b) 50, (c) 40, (d) 30, (e) 20, (f) 10, and (g) 5 ng $mL^{-1}$ at a scan rate of 100 mV $s^{-1}$, and (C) peak current of CEA *vs.* concentration ($R^2 = 0.982$). Adapted with permission from ref. 75. Copyright© 2014 Elsevier.

impedance—the sum of the real and imaginary impedance components—is obtained as a function of frequency ($f$) over a range of frequencies.[55] Resistance or capacitance that occurs at the electrode/electrolyte surface, is very sensitive to biological binding events, and therefore is effective for quantitative analysis of antigen–antibody reactions for label-free biosensor applications. Conductometric detection measures the ability of an analyte (*e.g.* electrolyte solutions) or a medium (*e.g.* nanowires) to conduct an electrical current, and can be regarded as a subset of impedimetric detection. However, this method is strongly associated with enzymes and therefore will not be further discussed herein.

In a semiconductor field effect transistor (FET), which includes source, drain, and gate electrodes, changes in the surface-charge density on its gate surface are detected. These changes are caused by the intrinsic charge of the adsorbed biomolecules.[56] The semiconductor channel is bridged by source and drain electrodes while the channel conductance is modulated by the gate electrode. Biorecognition takes place between the target analytes and the biological receptors, *e.g.* – antibodies, that are anchored to the semiconductor channel surface *via* chemical modification in the buffer environment. The surface potential of the semiconductor channel is varied and the channel conductance is modulated by the target–receptor interactions, and the signals are then collected by a detection system.[57]

For the detection of antigens using nanosensors, antibodies are usually immobilized onto an electrode surface, which can cause a severe biological activity loss.[43] Since the activity of surface immobilized antibodies depends on their orientation,[58] it is advantageous to assure that they are not randomly oriented. Other reasons for inactivity include steric hindrance in cases where an unreasonably high loading is used, denaturation due to non-specific interactions with the surface, as well as inappropriately high applied potentials.[59] Immobilization techniques include micro-contact printing, biotin–streptavidin binding, direct spotting, adsorption to a conductive polymer matrix such as polypyrrole[53] or polyaniline[60–62] as well as covalent binding.[63,64] Electrochemical enzymatic biosensors can be built up similar to the enzyme-linked immunosorbent assays (ELISAs). In this technique—after immobilizing antibodies to a surface—an analyte is introduced, which binds to the antibodies specifically. In the most common detection scheme, called a "sandwich" ELISA, a secondary labeled antibody then binds to the analyte in order to detect its concentration. These detection antibodies are coupled to an enzyme, which allows for quantitative measurements of the bound antigens by monitoring the electrical signal generated by the enzymatic reaction. The secondary antibody can also be fluorescently labeled and used in optical nanosensors (discussed in a later section).

Nanomaterials with high aspect ratio provide much more surface area for biomolecules interactions while remarkably reducing the instrumentation size, allowing for greater portability, reducing the amount of sample, and often reducing the lower limit of detection (LLOD).[65] Recently, electrochemical sensing platforms have been extensively investigated for

 

detecting various analytes by combining different electrochemical techniques with nanomaterials, such as nanostructured carbon[66–68]—including fullerenes and other carbon allotropes (*e.g.* – graphene)—quantum dots,[69] and noble metal nanoparticles,[70] which endow the biosensors with increasing water solubility and electrode surface area.[71,72] The following section will review recent developments made in the area of electrochemical-based antibody nanosensors.

### 2.1 Cyclic voltammetry (CV)

CV techniques have been used widely for the detection of biomarkers—characteristic factors measured or observed that serve as indicators of normal biological or pathogenic processes—as well as pharmacological responses to certain therapies in patients.[73] The measurement of protein biomarker levels in blood serum has been shown to hold promising potential for early cancer detection and treatment monitoring.[74] Electrochemical antibody nanosensors have attracted enormous attention with their high sensitivity and specificity, and relatively simple instrumentation. Whereas the traditional methods—including enzyme-linked immunosorbent assay (ELISA), radioimmunoassay (RIA), electrophoretic immunoassay, and mass spectrometry based proteomics—typically require sophisticated instrumentation, larger quantity of samples, limited sensitivity, high clinical expenses, and long experimental method times. Two types of antibody, a tracer (or detection antibody) and an intermediate primary antibody (or capture antibody), are usually involved in an electrochemical detection. The tracer labeled with an electroactive species, for example, an enzyme, metal nanoparticle, or quantum dot will bind with an analyte through the primary antibody, and is thus immobilized onto the sensing electrode surface to produce electrochemical signals for specific analyte detection.

Jin *et al.*[75] have fabricated multi-nanomaterial electrochemical biosensors based on magnetic beads (MBs), graphene (GR), and gold nanoparticles (AuNPs) to detect carcinoembryonic antigen (CEA) with a rapid response time, high sensitivity and specificity, and stability from the CV signals in the sensor. The multi-nanomaterial electrochemical biosensor integrates the merits of fast reaction kinetics along with high surface area per unit volume (a characteristic of their nanoscale diameters), and stability of the MBs.[76] These sensors also incorporate the fast electron transportation and biocompatibility of GR, and interesting physicochemical properties of AuNPs,[76] for example, the capability to conjugate with biomolecules (DNA, antibodies, enzymes). MBs-Ab1 are prepared by

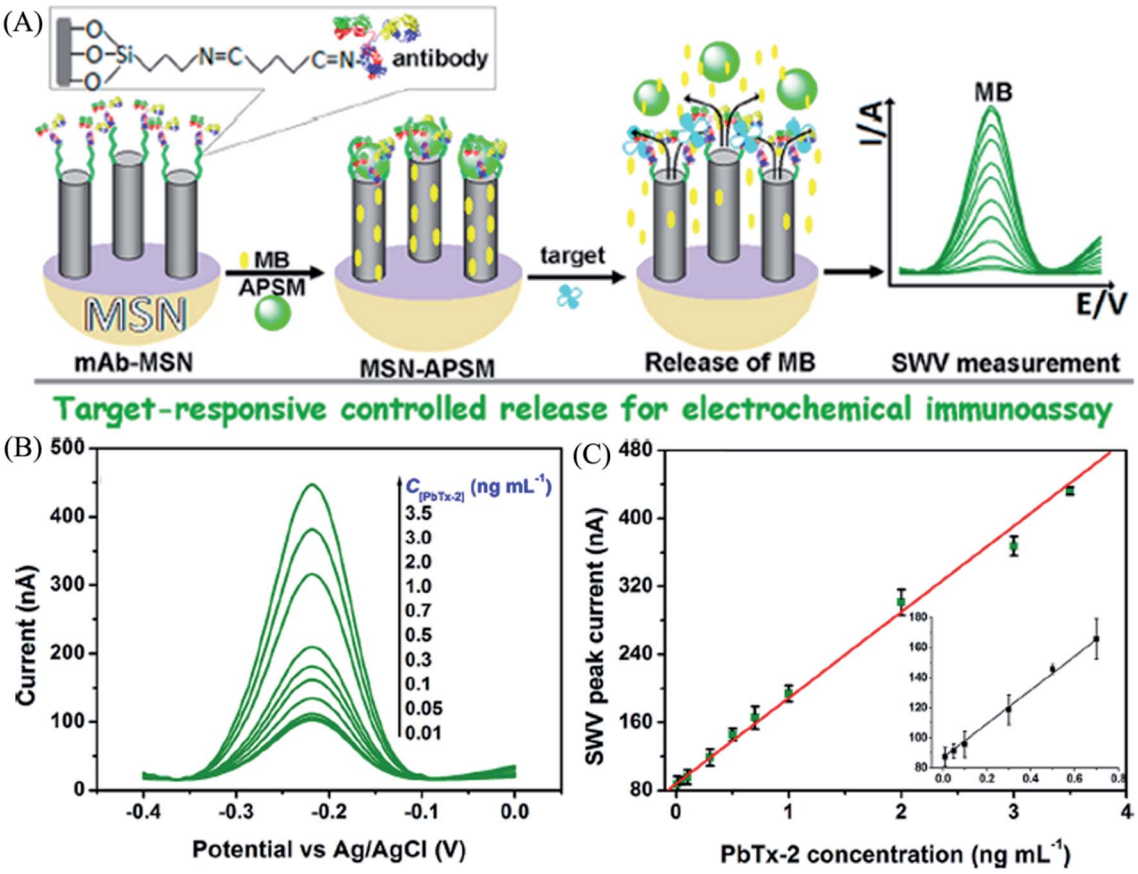


Fig. 3 (A) Working principles of the target-responsive controlled release for electrochemical immunoassay, (B) typical SWV response curves of the CRECIA-based immunoassays at different concentration of target PbTx-2 in PBS (pH 6.5), and (C) SWV peak currents *vs.* various target PbTx-2 concentrations. The potential was scanned from −400 to 0 mV (*vs.* Ag/AgCl, the amplitude is 25 mV, the frequency is 15 Hz, increase of *E* is 4 mV). Adapted with permission from ref. 78. Copyright© 2013 American Chemical Society.

coating MBs with capture antibodies and being attracted to isolated GR sheets by an external magnetic field, which innovatively acted as a conducting electrode with high specific surface area. The Ab2–AuNPs–HRP (AuNPs modified with horseradish peroxidase (HRP)—for signal amplification—and the detection antibody Ab2) is immobilized to the electrode through MBs Ab1 as illustrated in Fig. 2A. Anodic peaks in the CV curves (Fig. 2B) arising from the catalysis of $H_2O_2$ by Fe(III)-containing HRP giving rise to electrochemical signals for CEA detection. A linear relationship between the peak current at potential around 0.4 V and CEA concentration is obtained in the range of 5–60 ng $mL^{-1}$ in phosphate buffer solution (PBS, pH 7.4) containing 0.2 mM $H_2O_2$, Fig. 2C. The LLOD is found to be 5 ng $mL^{-1}$, however, detailed information regarding the capture and detection antibodies and the response time is not given in the paper.

### 2.2 Square Wave Voltammetry (SWV)

Recently, SWV has also been used for homogeneous immunoassays for small molecule detection in food safety and environmental monitoring. In contrast to heterogeneous immunoassays, homogeneous formats are superior in that no separation of a detectable specific binding member is needed, which eliminates the need for sample separation and complicated multistep washing. Compared to fluorescence or chemiluminescence techniques implemented in homogeneous immunoassays, electrochemical detection is a promising alternative as the next-generation detection strategy due to its high sensitivity, simple instrumentation, and excellent compatibility with miniaturization technologies. Carbolic methelyene blue (CMB), an organic redox indicator—which is blue when oxidized and colorless when reduced with a formal potential ranging from −0.10 to −0.40 V *vs.* SCE in pH 4–11 mediums[77]—has been reported to serve as an electroactive species to obtain electrochemical signals for direct readout. To further simplify the assay procedure, Zhang *et al.*[78] have developed a controlled release system based electrochemical immunoassay (CRECIA) for quantitative detection of PbTx-2 (brevetoxin B), a neurotoxin produced by algae, which can bring disruption of normal neurological processes and cause illness clinically described as neurotoxic shellfish poisoning. The detection is based on target-responsive controlled release of CMB from a polystyrene microsphere-gated mesoporous silica nanocontainer. CMB is first loaded into the pores of mesoporous silica functionalized by monoclonal mouse anti-PbTx-2 antibody (IgG) by stirring, and the pores are then capped with aminated polystyrene microspheres (APSM) through electrostatic forces between the negative charged antibodies in the former and the positive $-NH_3^+$ groups in the latter. The molecular gate is opened upon the introduction of the target, resulting in the release of MBs from the pores, as seen in Fig. 3A. The released MBs can be quantitatively tracked by square wave voltammetry (SWV) without sample separation or a washing procedure (Fig. 3B). Based on the target-responsive controlled release of MB mechanism, a correlation between

Table 1 Overview of discussed antibody nanosensors' transduction/detection methods and LLODs[d]

| Transduction method | Antibody or antibodies used for detection | Analyte(s) | Lower limit of detection (LLOD)[a] [ng $mL^{-1}$]{reported} | Ref. |
|---|---|---|---|---|
| Electrochemical | Anti-CEA | CEA | 5 | 75 |
| | Monoclonal mouse anti-PbTx-2 | PbTx-2 | $6 \times 10^{-3}$ {6 pg $mL^{-1}$} | 78 |
| | Polyclonal rabbit anti-CRP and polyclonal rabbit anti-MPO | CRP and MPO | 1 (CRP) and 0.5 {500 pg $mL^{-1}$} (MPO) | 28 |
| | Mouse IgG to HSA | HSA | $3 \times 10^{-5}$ {$3 \times 10^{-11}$ mg $mL^{-1}$} | 80 |
| | RPB monoclonal S-113-7 | RBP | 18 (EIS) and 47 (DPV) | 81 |
| Optical | Monoclonal anti-biotin | Biotin | $4.9 \times 10^{-3}$ {$2.0 \times 10^{-11}$ M} | 86 |
| | Monoclonal Anti-PSA | PSA | {$2.8 \times 10^{-13}$ M} | 122 |
| | Anti-mouse IgG | PSA | $10^{-9}$ {$10^{-18}$ g $mL^{-1}$} | 92 |
| | Anti-X[b] to HRP | X[b] | {$3.5 \times 10^{-13}$ M} | 90 |
| | Monoclonal mouse anti-PSA and goat anti-human IgG-Fc specific | PSA and p24 | $10^{-9c}$ {$10^{-18}$ g $mL^{-1}$} | 88 |
| | Monoclonal anti-PSA | PSA | {$10^{-19}$ M} | 93 |
| | Human IgG | Anti-human IgG | {3.3 $10^{-11}$ M} | 94 |
| Magnetic | Anti-mouse Saa1 and anti-mouse Flt3lg | Saa1 and Flt3lg | 3 (Saa1) and 0.04 {40 pg $mL^{-1}$} (Flt3lg) | 99 |
| | Monoclonal mouse anti-human PSA | PSA | 0.03 | 100 |
| | Anti-BChE | BChE | 6.5 {0.1 nM} | 101 |
| | Monoclonal murine Anti-cTnI | cTnI | 0.7 {30 pM} | 102 |
| Piezoelectric | Monoclonal mouse anti-$AFB_1$ (MIgG) and goat anti-MIgG | $AFB_1$ | 0.01 | 113 |
| | Anti-human IgG | Human IgG | 6.9 | 121 |

[a] The LLODs are normalized—for easy comparison—to ng $mL^{-1}$ (~ppm), if possible, and the reported values—if in different units—are also listed in braces. [b] X = a secondary monoclonal antibody that binds clinically relevant antigens in a sandwich assay. [c] These analytes have the same LLOD, using the reported antibody nanosensor. [d] Abbreviations used: lower limit of detection (LLOD), carcinoembryonic antigen (CEA), brevetoxin B (PbTx-2), C-reactive protein (CRP), myeloperoxidase (MPO), human serum albumin (HSA), retinol-binding protein (RBP), electrochemical impedance spectrotroscopy (EIS), differential pulse voltammetry (DPV), horseradish peroxidase (HRP), prostate specific antigen (PSA), immunoglobulin (IgG), crystallizable fragment (Fc), serum amyloid A1 (Saa1), Flt3 ligand (Flt3lg), butyrylcholinesterase (BChE), cardiac troponin I (cTnI), aflatoxin $B_1$ ($AFB_1$), and colony forming unit (CFU).

 

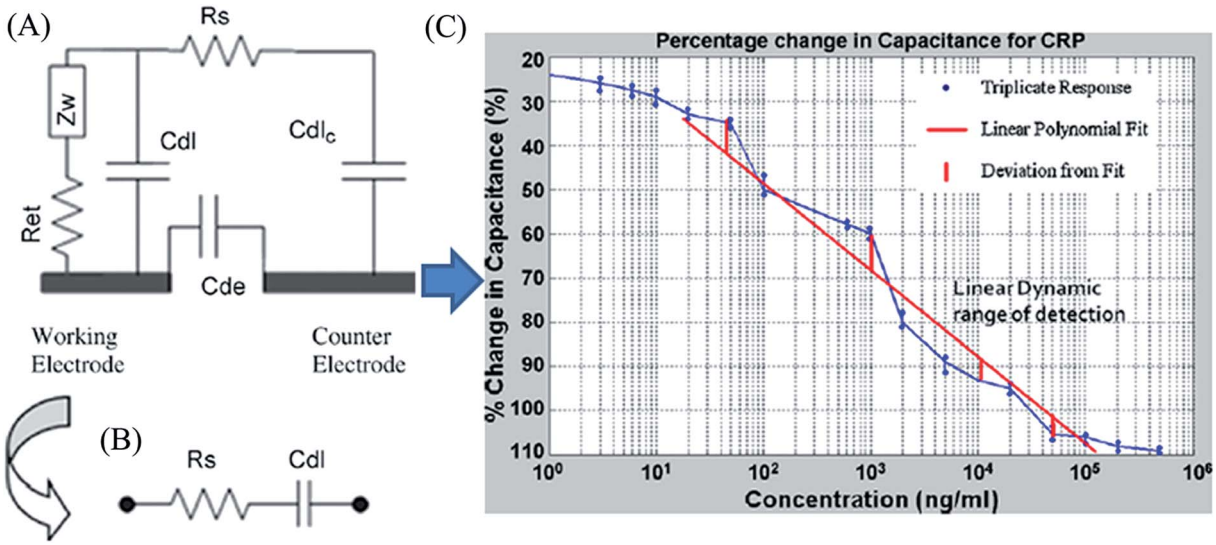


Fig. 4 (A) Equivalent electrical circuit across the electrodes following Randles cell model, (B) simplified final equivalent circuit, and (C) percentage change in capacitance at 1 kHz for dose response of CRP. Adapted with permission, from ref. 79. Copyright© 2010 Elsevier.

the SWV current and the PbTx-2 concentration can be established. A linear relation between the SWV current and the PbTx-2 concentration is achieved ranging from 0.01 to 3.5 ng $mL^{-1}$ in PBS (pH 6.5) (Fig. 3C) (Table 1).

An optimal experimental condition with 60 mg $L^{-1}$ $MB^{-1}$, 30 mg $mL^{-1}$ APSM, and 80 minutes for MB release at a $C_{[MSN]} \approx 10$ mg $mL^{-1}$ in the CRECIA is established. This simple, enzyme-free, label-free, and user-friendly method can obtain a lower limit of detection (LLOD) of 6 pg $mL^{-1}$ PbTx-2 at the $3S_{blank}$ criterion. The CRECIA also exhibits an acceptable specificity and reproducibility. The CRECIA is also applied to real samples—*i.e.*, three types of seafood samples—confirming the feasibility of the biosensors by comparing with commercialized PbTx-2 ELISA kit.

### 2.3 Electrochemical Impedance Spectrotroscopy (EIS)

EIS, one subclass of impedimetric technology, is an important tool for biomarker detection for cardiovascular disease (CVD)—the cause of nearly half of all deaths in the western world and over half of all deaths in Russia.[79] Given its high sensitivity to surface charge variations, iridium oxide is found to be highly suitable for electrochemical detection of biomolecules. Venkatraman *et al.*[28] have reported the use of iridium oxide nanowires to fabricate nanosensors wherein an immunoassay is built onto the iridium oxide nanowires.

The nanosensor is based on the formation and perturbation of the electrical double layer (EDL) formed at the iridium oxide nanowires/electrolyte interface. The protein binding to the antibody-saturated nanowires taking place at the interface will induce a perturbation in the EDL, and accordingly gives rise to a change in the capacitance of the EDL, $C_{dl}$. At lower frequencies, the equivalent circuit in the Randles cell model, Fig. 4A, will be reduced to a series combination of $R_s$ and $C_{dl}$, Fig. 4B. Therefore, the change in the impedance of the cell will be completely attributed to the change in the $C_{dl}$—making it possible to quantify the concentrations of the protein binding using EIS measurement. The EIS is performed under a DC bias of 200 mV and the detection of two cardiovascular disease biomarkers, inflammatory proteins C-reactive protein (CRP) and Myeloperoxidase (MPO), have been demonstrated. A linear trend is observed from 10 to $10^5$ ng $mL^{-1}$ for CPR, Fig. 4C, and 1 to $10^3$ ng $mL^{-1}$ for MPO. The LLOD is up to 1 ng $mL^{-1}$ for CRP and 500 pg $mL^{-1}$ for MPO in pure and serum sample, respectively. However, there are limitations existing, for example, the

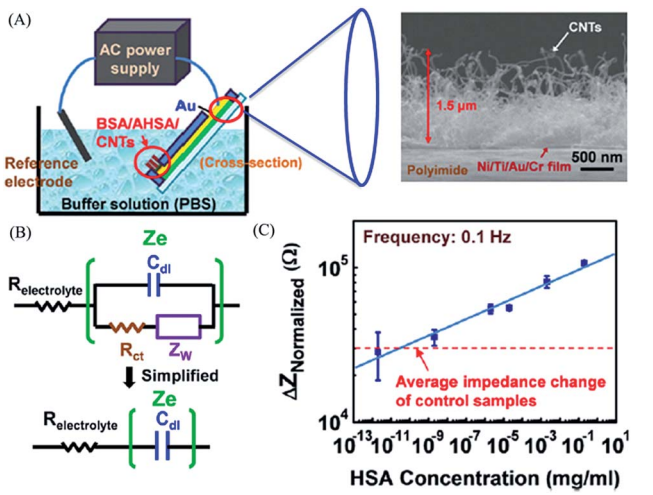


Fig. 5 Schematic diagram of the measuring system and its electrical measurement on a CNT biosensor. Equivalent circuit of the system based on the Randles and Ershler model and the equivalent circuit after simplification with only $R_{electrolyte}$ and $C_{dl}$. Impedance changes between pre- and post-HSA modification measured at 0.1 Hz *versus* HSA concentrations $N = 2$–3 for each HAS concentration with the average impedance change of control samples $N = 4$ indicated in the plot. ($\Delta Z_{Normalized} = (Ze_{BSA+AHSA} - Ze_{HSA+BSA+AHSA}) \times A$, where $A$ is the area of CNT-sensing region.) Adapted with permission from ref. 80. Copyright© 2013 Elsevier.

non-specific binding and cross-reactivity, which constrained the detection limit. It is suggested that higher sensitivity could be accomplished *via* specific biochemical functionalization of the nanowire surfaces with customized proteins for the binding and detection of specific proteins, as well as reducing noise, and enhancing through put from multiple detection sites.

Similarly, Chang *et al.*[80] have demonstrated the feasibility of CNT flexible biosensors by observing a change in the EDL capacitance, $C_{dl}$, for the detection of human serum albumin (HSA)—which is frequently used to monitor liver function. The utilization of carbon nanotubes (CNTs) can be attributed to their high surface-to-volume ratio, excellent electrical conductivity, and mechanical strength, which are beneficial for obtaining highly sensitive nanosensors. A flexible substrate also makes the biosensor more portable, robust, and biocompatible, rendering it promising in various applications. The CNTs are grown directly on a polyimide flexible substrate at low temperature while AHSA (mouse IgG antibody to HSA) is covalently bound onto the CNTs *via* self-assembled amine coupling chemistry (Fig. 5A). BSA blocking of untreated and non-specific bonding is performed to enhance the detection specificity before HSA sensing. The impedance is conducted in a PBS solution with an AC voltage of 10 mV. In the same manner, the equivalent circuit simplifies at low frequencies, as seen in Fig. 5B. HSA concentration can be correlated to the increase of $C_{dl}$ at 0.1 Hz, which indicates the capacitive impedance in an EIS measurement. A linear slope is obtained at HAS concentrations ranging from $2 \times 10^{-1}$ to $3 \times 10^{-11}$ mg mL$^{-1}$ with a detection limit of approximately $3 \times 10^{-11}$ mg mL$^{-1}$ HAS at 0.1 Hz, Fig. 5C. A limitation of the sensors is that the background impedance must be controlled at a certain value to stabilize the background signal, otherwise, there will be large variations in the result. In addition, the purity of CNTs is not as high as those grown at higher temperatures.

### 2.4 Differential Pulse Voltammetry (DPV) combined with EIS

Combined voltammetry and EIS techniques have also been used to detect specific biomarkers. Urinary retinol-binding protein

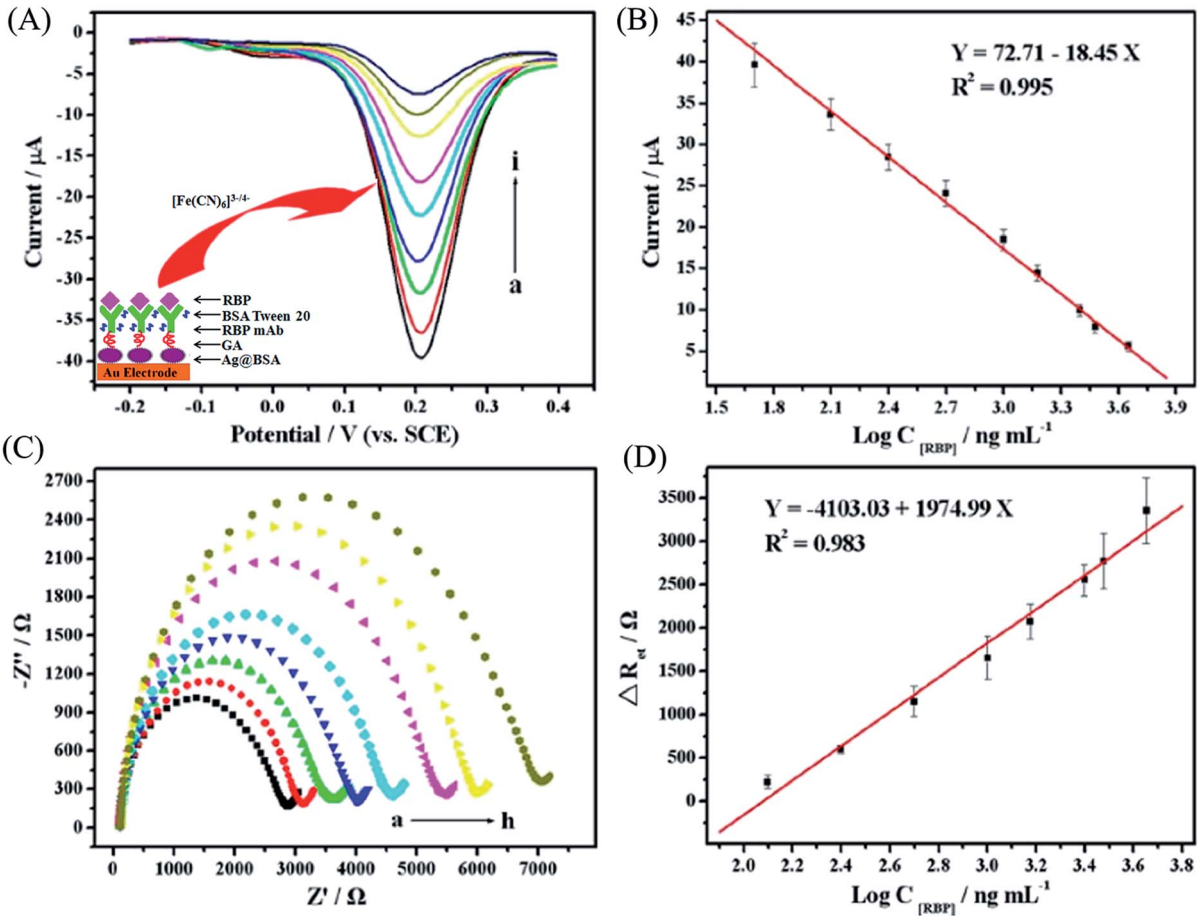


Fig. 6 Typical DPV and EIS results for immunosensors incubated with RBP standard in 5 μL of PBS (10 mM, pH 7.4) for 1 h and washed with PBST and PBS. (A) Typical DPV response of electrochemical immunoassay in 10 mM, pH 7.4 PBS containing $[Fe(CN)_6]^{3-/4-}$(10 mM, 1 : 1) and 0.1 M KCl with increasing RBP concentration from (50, 125, 250, 500, 1000, 1500, 2500, 3000, 4500 ng mL$^{-1}$ RBP, respectively). (B) The resulting calibration curve between the DPV peak current (corrected for background) and the logarithm values of RBP concentrations. (C) EIS response of electrochemical immunoassay with increasing RBP concentration (125, 250, 500, 1000, 1500, 2500, 3000, 4500 ng mL$^{-1}$ RBP, respectively) (using the same conditions as in Fig. 2A). (D) The calibration curve of the impedance immunosensor for detecting RBP. Adapted with permission from ref. 81. Copyright© 2012 American Chemical Society.

 

(RBP) is a biomarker for renal tubular injury and is very important for early detection of proximal tubular dysfunction, which is closely associated with some serious diseases such as diabetes mellitus and hypertension. Immobilizing RBP monoclonal antibody on Ag@BSA microspheres for the highly sensitive detection of urinary RBP has been conducted by Hu *et al.*[81]

The large surface area of Ag@BSA and attached BSA molecules are able to enhance the amount of antibodies (IgG) and, hence, antigens immobilized on the modified electrode, while keeping the bioactivity of these immobilized biomolecules. In addition, the inner Ag nanoparticles will improve the electrochemical sensing ability by acting as an electrical conductor. Both DPV and EIS are employed to evaluate the nanosensor performances. From the peak currents in the DPV measurement, Fig. 6A, a linear relationship is obtained at $\log(C_{RBP})$ ranging from 1.5 to 3.9 ng $mL^{-1}$, Fig. 6B, with a LLOD of 18 ng $mL^{-1}$. From EIS, Fig. 6C, a linear slope is achieved at $\log(C_{RBP})$ ranging from 2.0 to 3.8 ng $mL^{-1}$, Fig. 6D, with a LLOD of 47 ng $mL^{-1}$, which is slightly higher than the DPV measurement. The broader detection range and lower detection limit of RBP, indicate limitless potential in clinical diagnosis.

# 3. Optical antibody nanosensors

Recently, optical (derived from the Greek *optikos* meaning "of or having to do with sight") nanosensors attract more and more interest due to their outstanding detecting performance, such as high sensitivity,[72] label-free techniques,[82] and real-time monitoring capabilities.[83] Optical sensing technology is based on monitoring changes in the refractive index in the proximity of the sensor surface. In comparison to their conventional electronic counterparts, optical biosensors offer several advantages, such as long distance sensing and the possibility of multiplexing several sensing channels.[84]

Many of the most widely used optical nanosensors are based on the phenomenon of surface plasmon resonance (SPR) techniques, which includes localized surface plasmon resonance (LSPR) and interference localized surface plasmon resonance (iLSPR).[85] The LSPR is based on monitoring the nanoparticle extinction peak ($\lambda_{max}$) shift from the UV-visible spectra. The $\lambda_{max}$ value depends on the local refractive index at the nanoparticle surface, which changes with biomolecular binding to specific-bound ligands.[86] The LSPR sensors can monitor binding events in real time and detect a variety of processes, however, the sensitivity of the LSPR decreases with longer surface ligands.[86] The challenges for using the optical nanosensors are focused on how to increase the sensitivity to detect single-molecules and how to develop instrumentation for routine use.

Another type of optical nanosensor that is widely used is based on enzyme linked immunosorbent assays (ELISA)—similar to those mentioned in section 2.1. Electrochemical antibody nanosensors—which use labels to detect immunological reactions.[87] In conventional ELISA the color is generated by the conversion of the enzyme substrate into a colored molecule, and the intensity of the solution is quantified by measuring the absorbance with a plate reader.[88] However, conventional ELISA includes a tedious and labor-intensive protocol—demanding many mixing (reaction/incubation) and washing steps—that often leads to human-error and inconsistent results. This can often make performing one assay take hours, and is attributed to the long incubation times during each step.[89] The aforementioned methods can be combined together to improve the performance of the optical nanosensor. By measuring the shift of the LSPR $\lambda_{max}$ caused by the enzymatic activity of target molecules per single particle, a new method providing a basis for further development of simple and robust colorimetric bioassays with single molecule resolution can be recognized.[90] In order to enhance the sensitivity of plasmonic sensors, several methods have been applied to enhance the wavelength shift of the LSPR nanosensor.

## 3.1 Plasma oscillations

Plasmonically active nanoparticle labels are applied to achieve increased sensitivity of the nanosensors by enhancing the wavelength shift upon biomolecule binding.[86] Here, nanoparticle-antibiotine conjugates with a concentration range of 20 pM to 1 μM are incubated with the biotine-functionalized nanoprism arrays for 45 min. Here, a peak shift ($\Delta\lambda_{max}$) of 11 nm is observed in the LSPR spectra by using native antibiotin, however for the gold nanoparticles labeled antibiotin, the $\Delta\lambda_{max}$ can reach 42.7 nm, which is increased 400% compared with $\Delta\lambda_{max}$ of the native antibiotin. However, the NP–antibody conjugates show disadvantages, such as aggregation, nonspecific adsorption or binding, size variation, and lack of stability.[91] Enzyme glucose oxidase is also introduced to obtain the enhanced wavelength shift of the LSPR nanosensor.

Rodríguez-Lorenzo *et al.*[92] have successfully enhanced the sensitivity of LSPR by introducing the enzyme glucose oxidase (GOx), which can control the crystal growth of silver ions on the gold nanosensors *via* favoring either additional nucleation or growth of existing nanocrystals. As shown in Fig. 7, with lower concentrations of GOx, silver would grow on the surface of gold nanostars and lead to a blue shift in the LSPR. However, with high concentrations of GOx, silver tends to form freestanding silver nanocrystals, and limited silver would grow on the nanosensor causing smaller LSPR shifts. By modifying with GOx, the signal of the gold sensor is sensitized with less concentration of the target molecule. The sensitivity of the plasmonic nanosensors is tested through the detecting of prostate specific antigen (PSA). The gold nanostars modified with polyclonal antibodies against PSA is first incubated with PSA for 2 hours, and then the captured PSA on the surface of the particles are further detected with monoclonal antibodies and labeled with secondary antibodies bound to GOx. Finally, the obtained GOx-nanoparticles are applied to trigger the nucleation of the Ag. The result shows that the limit of detection (lowest concentration of analyte in the inverse-sensitivity regime) can reach $10^{-18}$ g $mL^{-1}$.

In order to improve the performance of the optical nanosensors, LSPR and ELISA methods are combined, by measuring the shift of the LSPR $\lambda_{max}$ caused by the enzymatic activity of target molecules per single particle. This new method provides a basis for further development of simple and robust

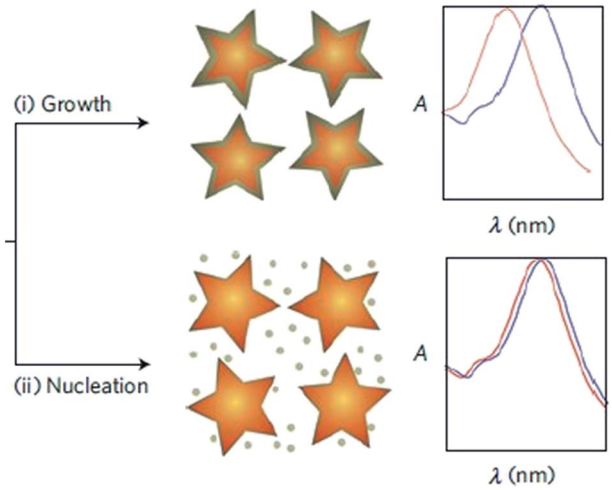


Fig. 7 Scheme of the proposed signal-generation mechanism by means of enzyme-guided crystal growth. (i) GOx is present at low concentrations; (ii) at high concentrations. Reproduced with permission from ref. 92. Copyright© 2011 American Chemical Society.

colorimetric bioassays with single molecule resolution.[90] For further improving the sensitivity of the LSPR nanosensor, an enzyme-catalyzed precipitation reaction is applied to enhance the peak shift. $H_2O_2$ and then insoluble precipitate will be formed around the catalytic site (Fig. 8C). The peak shift is shown in Fig. 9A, where, by using this combination method, the much smaller $\lambda_{max}$ shift induced by the HRP adsorption itself ($\Delta\lambda_{HRP}$) is related to the $\lambda_{max}$ shift caused by the enzymatic precipitation ($\Delta\lambda_{product}$). The number of HRP molecules (#HRP) per particle is then corresponded to a certain peak shift $\Delta\lambda_{HRP}$, thus, the $\Delta\lambda_{product}$ can be further converted to #HRP. This is shown in B, where the colorimetric response is enhanced up to 50 times by applying the enzymatic reaction.

LSPR sensing with elliptical Au nanodisk arrays has been fabricated *via* thermal nanoimprint lithography (NIL), with the addition of enzyme–antibody conjugates to enhance the sensitivity of the detection of the PSA.[91] The morphology of the optically anisotropic elliptical Au nanodisk arrays is studied by SEM, as shown in Fig. 10A and B. Here, the long-axis and short axis of the Au nanodisk are named as $I_i$ and $I_s$, which show different extinction peaks (Fig. 10C).

The obtained elliptical Au nanodisks are first modified with 11-mercaptoundecanoic acid (MUA), shown in Fig. 11A, and then the functionalized nanodisks are incubated in solution of anti-PSA to immobilize the antibody (Fig. 11B). After that the PSA, biotinylated anti-PSA and streptavidin–alkaline phosphatase is applied to form the sandwich assay (Fig. 11C and D). Finally, the enzyme-catalyzed precipitation reaction will take place and yield insoluble precipitates onto the nanodisk surfaces (Fig. 11E and F).

The LSPR spectra[91] without the enzymatic precipitation, the detection of PSA is difficult with a concentration of PSA as low as 2.8 nM, however, by introducing enzymatic precipitation at a concentration of 280 fM of PSA is detectable with only a 4.7 and 5.5 nm shift in the s-peak and l-peak, respectively. This

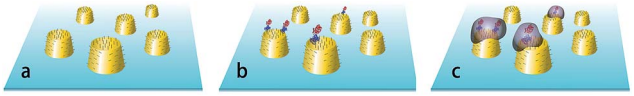


Fig. 8 Schematic representation of the experiment. (A) Dispersed, biotinylated, gold nanoparticles are studied on glass substrates, (B) streptavidin–HRP bind with biotin and (C) precipitation reaction on the particle surface. Reproduced with permission from ref. 90. Copyright© 2011 American Chemical Society.

combined method of LSPR and ELISA can also achieve naked eye detection.

In conventional colorimetric ELISAs, the target molecule is captured by antibodies labeled with enzyme and the conversion of enzyme generates a colored signal, however, the intensity of the color being detected with the naked eye is limited by the concentration of the target molecule.[88] Plasmonic ELISA methods are applied for detecting a small number of molecules of analyte with the naked eye.[88] The growth of gold nanoparticles that generated the colored solution is controlled by the enzyme label of an ELISA in the presence of analyte. A

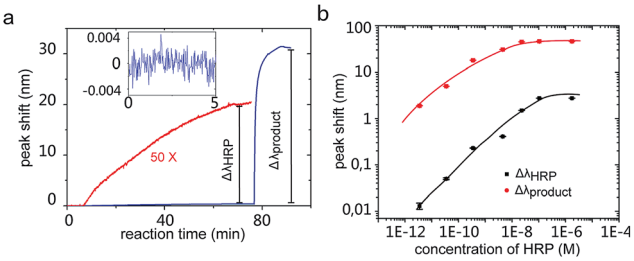


Fig. 9 (A) Peak shift *vs.* time during binding of SA-HRP (red curve, multiplied by a factor 50) and precipitate formation on particle surface (blue curve) induced by HRP induced. The inset shows the baseline variation before introducing HRP. (B) Peak shifts *vs.* HRP concentration, induced by SA-HRP and corresponding enzyme (the lines are guides to the eye only). Reproduced with permission from ref. 90. Copyright© 2011 American Chemical Society.

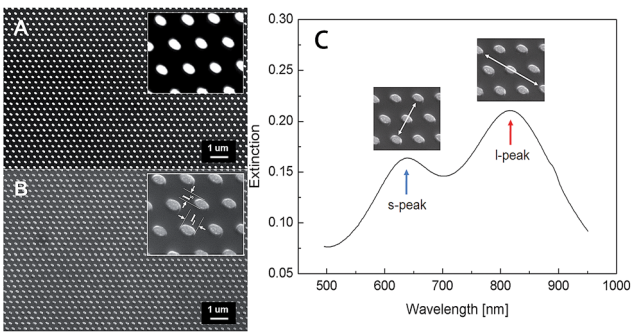


Fig. 10 SEM images of (A) the array pattern of the elliptical Si nanopillars on an LIL stamp, and (B) the array pattern of elliptical Au nanodisks fabricated on a glass wafer; extinction spectrum of (C) as-prepared elliptical Au nanodisk arrays, including s-peak and l-peak. Reproduced with permission, from ref. 91. Copyright© 2011 American Chemical Society.

conventional colorimetric ELISA with a biotin–streptavidin linkage, where the target molecule is first captured by specific antibodies and then labelled with an enzyme, is shown in Fig. 12A. For the plasmonic ELISA, the growth of gold nanoparticles to obtain blue- or red-colored solutions is linked with the biocatalytic cycle of the enzyme with or without the analyte, respectively (Fig. 12B).

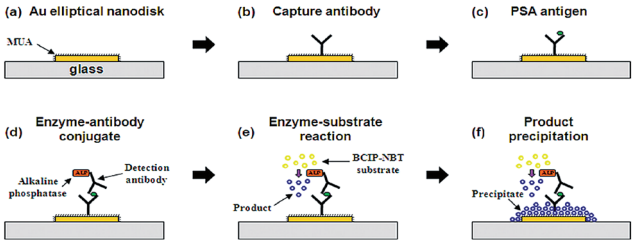


Fig. 11 Schematic illustration of PSA detection procedure, (A) Modification with MUA. (B) Immobilization of the PSA antibody. (C) Binding of PSA to the antibody. (D) Sandwich binding of alkaline phosphatase-detection antibody conjugate to PSA. (E) Enzymatic reaction of the BCIP/NBT substrate. (F) Product precipitation on the nanodisk. Reproduced with permission from ref. 91. Copyright© 2011 American Chemical Society.

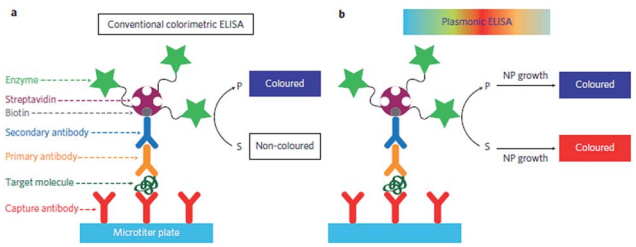


Fig. 12 The signal generation mechanism of (A) conventional colorimetric ELISA and (B) plasmonic ELISA. (S, substrate; P, product; NP, nanoparticle). Reproduced with permission from ref. 88. Copyright© 2012 Nature Publishing Group.

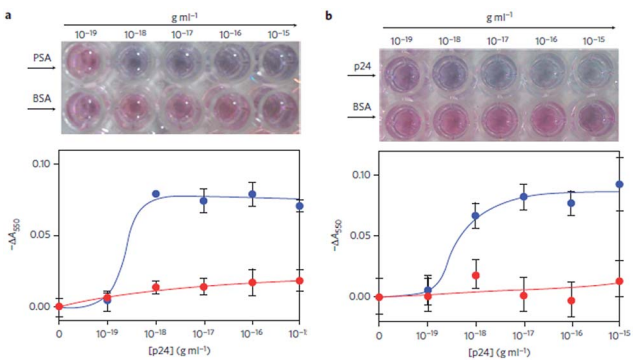


Fig. 13 Naked-eye detection of (A) PSA and (B) p24 with plasmonic ELISA. The growth of gold nanoparticles is monitored by measuring the absorbance at 550 nm, blue curves are obtained with PSA or p24, red curves are obtained without the target molecules. Reproduced with permission from ref. 88. Copyright© 2012 Nature Publishing Group.

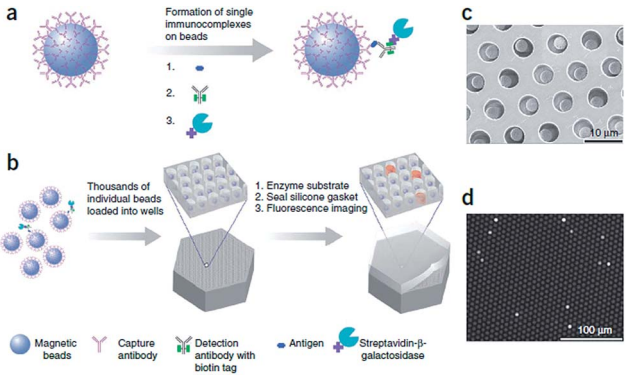


Fig. 14 Digital ELISA based on arrays of femtoliter-sized wells. (A) Single protein molecules are captured and labeled on beads using standard ELISA reagents. (B) Beads with or without a labeled immunoconjugate are loaded into femtoliter-volume well arrays for isolation and detection of single molecules by fluorescence imaging. (C) Scanning electron micrograph of a small section of a femtoliter-volume well array after bead loading. Beads (2.7 μm diameter) are loaded into an array of wells with diameters of 4.5 μm and depths of 3.25 μm. (D) Fluorescence image of a small section of the femtoliter-volume well array after signals from single enzymes are generated. Whereas the majority of femtolitervolume chambers contain a bead from the assay, only a fraction of those beads possess catalytic enzyme activity, indicating a single, bound protein molecule. The concentration of protein in bulk solution is correlated to the percentage of beads that carry a protein molecule. Reproduced with permission from ref. 93. Copyright© 2010 Nature Publishing Group.

The working mechanism of the gold nanoparticles is that without the analyte, the gold ions reduced rapidly in the presence of hydrogen peroxide and the solution shows a red color. With the analyte present, the hydrogen peroxide reacts with the

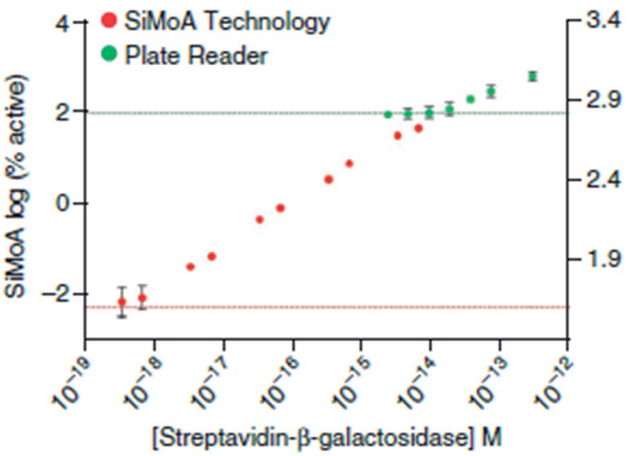


Fig. 15 log–log plot of signal output as a function of the concentration of streptavidin-β-galactosidase (SβG) captured on biotinylated beads. SβG concentrations for the ensemble readout ranged from 3 fM to 300 fM, with a detection limit of $15 \times 10^{-15}$ M (15 fM; green broken line). For the SiMoA assay, SβG concentrations ranged from 350 zM to 7 fM, demonstrating a linear response of ~10 000-fold, with a calculated detection limit of $220 \times 10^{-21}$ M (220 zM; red broken line). Reproduced with permission from ref. 93. Copyright© 2010 Nature Publishing Group.

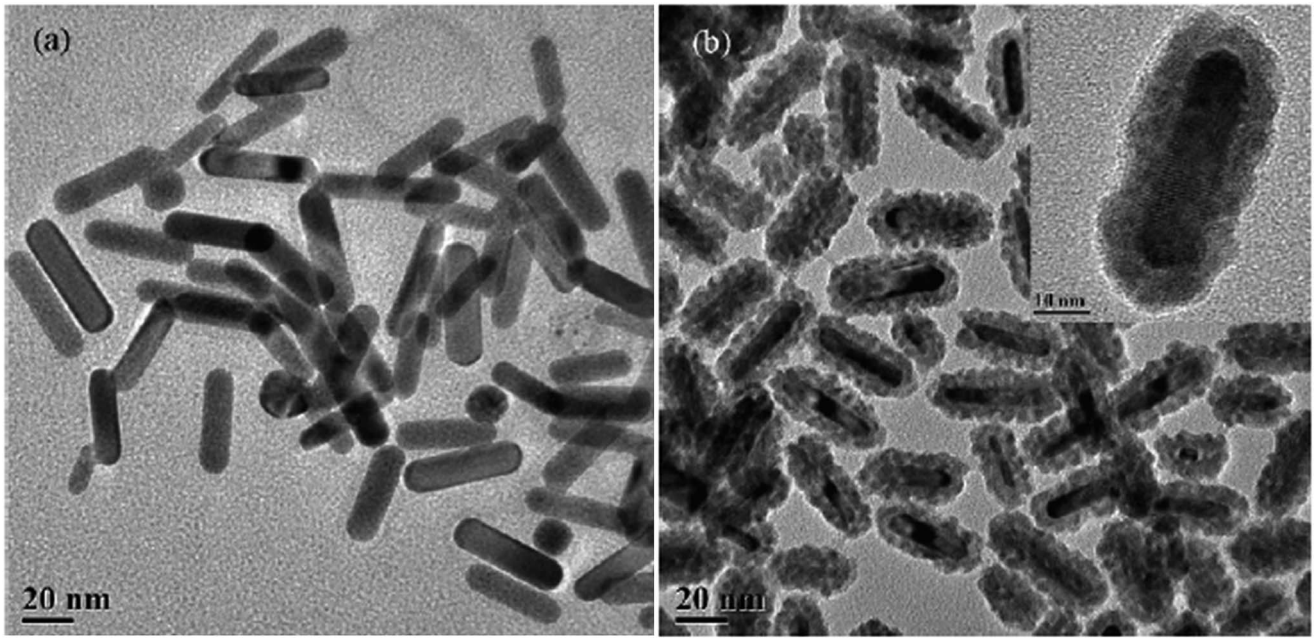


Fig. 16 TEM images of (A) as-synthesized gold nanorods and (B) $Au_2S$-coated GNRs. Reproduced with permission, from ref. 94. Copyright© 2009 Elsevier.

enzyme catalase, which leads to an ill-defined morphology of gold nanoparticles resulting in a blue color. The detection of the analyte with the naked eye is facilitated by the blue or red color change.

The plasmonic ELISA is applied to two model analytes: prostate specific antigen (PSA) and HIV-1 capsid antigen p24. Fig. 13 shows the results for the detection of PSA and p24 with plasmonic ELISA. In both cases, the limit of detection—which can reach down to $10^{-18}$ g $mL^{-1}$—is defined as the lowest concentration of analyte that yields a blue-colored nanoparticle solution. Here, the ability to detect single protein molecules in blood is significant for the diagnosis utilizing biomarkers.[93]

### 3.2 Fluorescent enzyme-linked immunosorbent assay (ELISA)

In order to detect proteins at low concentrations in blood, microscopic beads with specific antibodies are designed to capture the proteins. Once captured, the authors labeled the immunocomplexes (one or zero labeled target protein molecules per bead) with an enzymatic reporter capable of generating a fluorescent product. When the beads are isolated in small volume (~50 fL) reaction chambers—that are designed to hold only a single bead—single protein molecules can be detected by fluorescence imaging.[93]

As in a conventional bead-based ELISA, a sandwich antibody complex with an enzyme labeled antibody forms on microscopic beads (Fig. 14). At extremely low concentrations of protein, the ratio of protein molecules (and the resulting enzyme-labeled complex) to beads is small (typically <1 : 1), and the beads carry either a single immunocomplex or none. Here, the limited enzyme labels are unable to be detected by using standard detection technology (for example, a plate reader), because of the hundreds of thousands of enzyme labels that are required to create a fluorescence signal above background (Fig. 15).

In the developed digital ELISA method, however, the fluorophores generated by single enzymes can be confined, which allow for the detection of very low concentrations of enzyme labels. In order to obtain such a confinement, femtoliter-sized reaction chambers utilized in the digital ELISA approach are applied to trap and detect single enzyme molecules. Each bead is isolated in a femtoliter-volume reaction chamber, where it is possible to distinguish between the beads associated with a single enzyme molecule (identified as an "on" well) from those not associated with an enzyme (identified as an "off" well). By

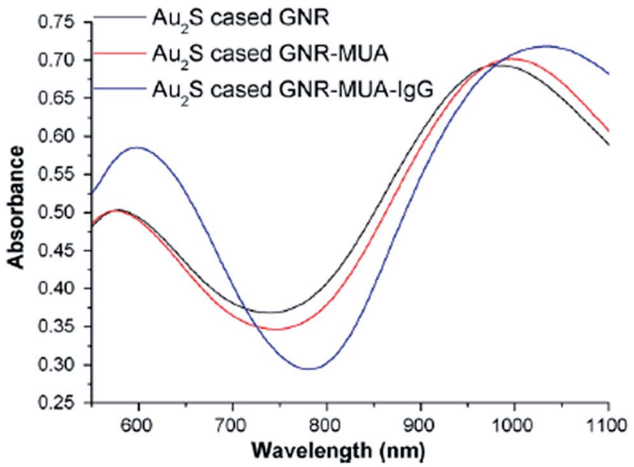


Fig. 17 Absorption spectra acquired from $Au_2S$-coated GNRs in turn attached with MUA and human IgG. Reproduced with permission, from Huang *et al.* ref. 94. Copyright© 2009 Elsevier.

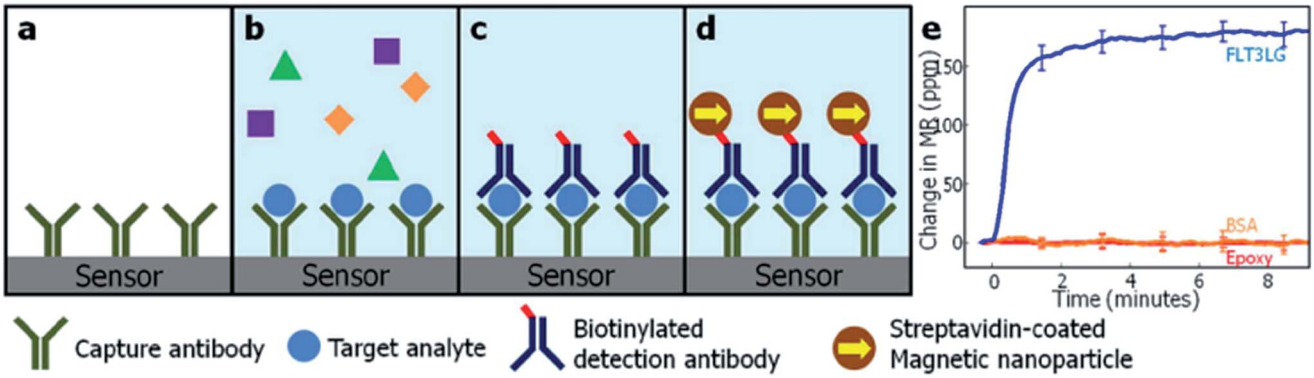


Fig. 18 (A–D) A schematic of magneto-nanosensor biochip immunoassay: (A) capture antibodies are immobilized covalently on the sensor surface. (B) Target antigens are capture and non-complementary antigens are subsequently washed away. (C) Addition of biotinylated detection antibody forms a sandwich structure. (D) Streptavidin-coated magnetic nanoparticles bound to the biotinylated detection antibody produce stray magnetic field. (E) An example of real-time binding curve showing the change in magnetoresistance (MR) in parts per million (ppm) over time for 500 pg $mL^{-1}$ Flt3lg (blue) compared with BSA negative control (orange) and epoxy reference (red). Error bars ±1 standard deviation. Reproduced with permission from ref. 99. Copyright© 2013 Elsevier.

counting the number of wells containing both a bead and fluorescent product relative to the total number of wells containing beads, the protein concentration in the test sample is obtained. As single-molecule arrays (SiMoAs) enable the concentration to be determined digitally rather than by using the total analog signal, the approach is called a digital ELISA.

By applying this single-molecule enzyme-linked immunosorbent assay (digital ELISA) approach, the authors are able to detect as few as ~10–20 enzyme-labeled complexes in 100 mL of sample (~$10^{-19}$ M), and is able to detect clinically relevant protein levels in serum at concentrations (<$10^{-15}$ M)—much lower than conventional ELISA (Fig. 5).[93] Although, the LSPR and ELISA nanosensors show outstanding properties, both of them depend on a label, and among optical nanosensors there is only one type of label-free nanosensor.

### 3.3 Vis-NIR spectroscopy

$Au_2S$-coated gold nanorods ($Au_2S$-coated GNRs) are prepared, as can be seen in Fig. 16.[94] The $Au_2S$ shell can easily react with mercaptoundecanoic acid (MUA) to form a self-assembled membrane (SAM), which can further covalently link with biomolecules. As shown in Fig. 17, a red shift of 9 nm is measured after attaching MUA on the $Au_2S$-coated GNRs—indicating the formation of SAM. When the formed $Au_2S$-coated GNRs with SAM of MUA is further reacted with human IgG, a red shift up to 40 nm is shown, which implies the successful attachment of human IgG on the surface of $Au_2S$-coated GNRs (Fig. 18).

The functionalized $Au_2S$-coated GNRs are applied to detect the goat anti-human IgG and the limit of detection is studied with the steady-state response of the GNR sensor as a function of the sample concentration. The peak at 1055 nm is chosen as the signal indicator of target binding events in the range from 33 pM to 1.35 nM, the absorbance change is linearly proportional to the concentration, which indicating that the limit of detection is around 33 pM. In this section, several types of optical nanosensors with high sensitivity are presented and the results pave the way for the development of single molecule and simple detection, which would be more suitable for clinical environments.

## 4. Magnetic antibody nanosensors

Nanoparticles (NPs) are of great interest for sensors, as the conjugation of various biomolecules to different kinds of nanoparticles has led to the creation of hybrid bioorganic–inorganic nanocomposites that encompass bio-recognition capabilities as well as unique photonic, magnetic, or electronic properties—the fine modulation of which can be applied to a number of nanosensors.[95] Magnetic (a word derived from the Old French *magnete* meaning "magnetite ($Fe_3O_4$)") nanoparticles are a class of nanoparticles that can be manipulated *via* the influence of an external magnetic field. Magnetic NPs are widely used in magnetic resonance imaging, targeted drug and gene delivery, tissue engineering, cell tracking, and bioseparations.[3,95] Recently, magnetic nanoparticles have been widely used in antibody nanosensors, because of their high sensitivity, fast response, and reliability. The following section will discuss recent developments made in the area of magnetic nanoparticles used in antibody nanosensors with enhanced sensitivity, as well as introduce the morphology of a number of the magnetic antibody nanosensors.

### 4.1 Giant magnetoresistance (GMR)

Magneoresistance (MR) is a phenomenon that reflects the resistance change of a material under an external magnetic field.[53,60,66,96] Generally, the MR effect can be categorized into five distinct types, which include ordinary magnetoresistance (OMR), anisotropic magnetoresistance (AMR), giant magnetoresistance (GMR), tunneling magnetoresistance (TMR), and colossal magnetoresistance (CMR).[66] Giant magnetoresistance (GMR) is defined as: $MR\% = [R(H) - R(0)]/R(0) \times 100\%$, where $R(0)$ is the resistance without magnetic field, $R(H)$ is the resistance under an external magnetic field $H$.[97,98]

GMR nanosensors provide a novel approach for measuring protein concentrations in blood for medical diagnosis.[99] The method has high sensitivity, scalability, and multiplexing capability. Fig. 8 shows the detection strategy for blood proteins. The capture antibody immobilized onto a nanosensor surface. Once the antibody on the nanosensor surface captures the target antigens, the non-complementary antigens are subsequently washed away. After washing, the addition of biotinylated detection antibodies forms a sandwich structure. Here, the streptavidin-coated magnetic nanoparticles are bound to the biotinylated detection antibody. When an external oscillating magnetic field is applied, the stray fields induced from the bound magnetic nanoparticles allow for resistance changes in the GMR spin-value sensor located beneath the platform surface. The resistance changes are proportional to the local concentration of the nanoparticles on the sensor surface, and are measured in real-time using a custom electric read-out system.

### 4.2 Magnetic bead-based immunoassays

Recently, colorimetric immunoassays have gained great attention in various research areas such as biomedical diagnosis, food safety analysis, and environmental monitoring, due to several important advantages, such as simplicity, practicality, low cost, and rapid/direct readout with naked eye. There are many kinds of colorimetric immunoassays, such as aggregation-based, lateral-flow, and enzyme-mediated colorimetric immunoassays.[100] Among the various colorimetric immunoassays, enzyme-mediated colorimetric immunoassay have received a great deal of attention due to their high sensitivity and amplification of the signal, and, hence, have been applied to many different fields. Normally, horseradish peroxidase and alkaline phosphatase are the most widely used enzymes in the colorimetric immunoassay. Gao *et al.*[100] combined the ultrahigh catalytic activity of catalase with the advantages of the reverse assay model to exploit a novel signal generation method for developing a reverse colorimetric immunoassay with an enhancement in sensitivity. In this work, a novel reverse colorimetric immunoassay strategy (RCIA) is utilized for the sensitive detection of low-concentrations of protein (prostate specific antigen, PSA) in biological fluids by coupling highly catalytic efficiency catalase with magnetic bead-based peroxidase mimics. In order to construct such an RCIA system, the functionalization of the magnetic beads and gold nanoparticles is needed, as seen in Fig. 9A. The magnetic beads and gold nanoparticles are first synthesized and functionalized with anti-PSA capture antibody and cata/anti-PSA detection antibody, respectively. Fig. 9B shows the formed reverse enzyme colorimetric immunoassay. In the presence of target PSA, the sandwiched immunocomplex is formed between MB-Ab1 and multi-CAT-AuNP-Ab2. The carried CAT could catalyze the reduction of $H_2O_2$ in the detection solution, and consumed the partial $H_2O_2$, thereby showing down the catalytic efficiency of MB toward TMB/$H_2O_2$. As such, the absorbance is decreased and visible color weakened. By monitoring the decrease in the absorbance, we could quantitatively determine the concentration of target PSA in the sample. The detection limit is 0.03 ng $mL^{-1}$. Because the threshold of total PSA in normal humans is about 4 ng $mL^{-1}$, the developed RCIA can completely meet the requirement of the clinical diagnostics.

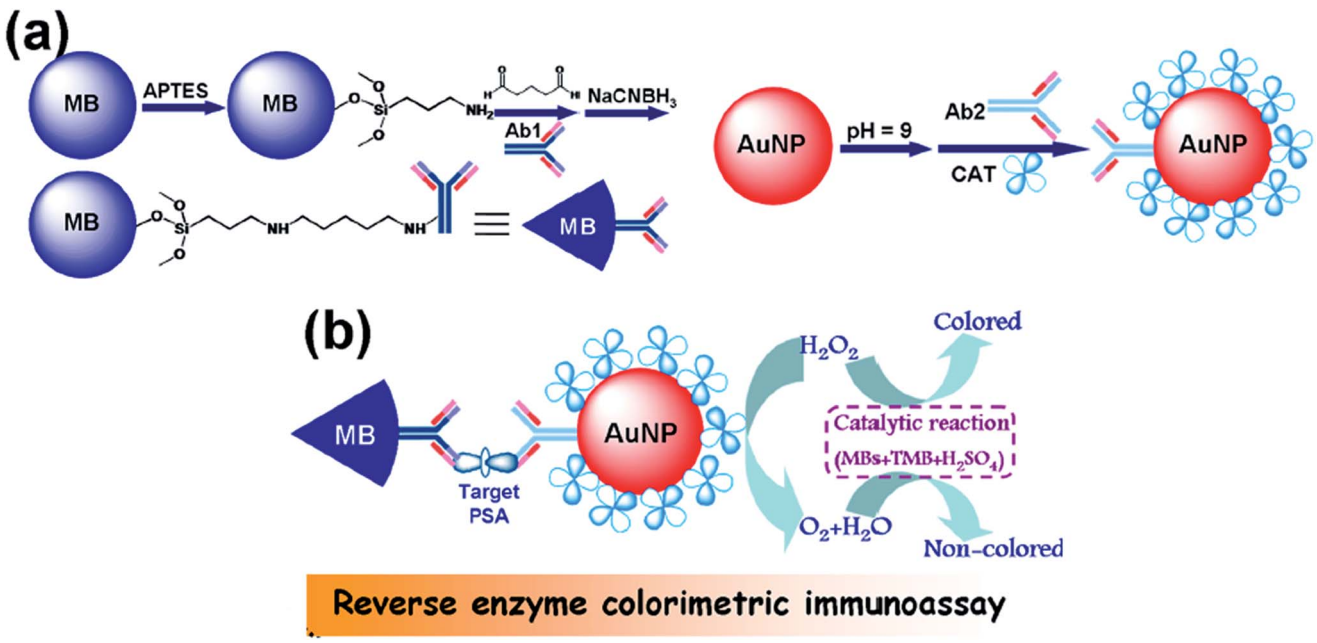


Fig. 19 Magnetocontrolled enzyme-mediated reverse colorimetric immunoassay protocol (A) design of monoclonal mouse anti-human PSA-conjugated magnetic beads (MB-AB1) and polyclonal goat anti-human PSA/catalase-labeled AuNP( multi-CAT-AuNP-Ab2), (B) magneto-controlled enzyme-mediated reverse colorimetric immunosensing strategy. Reproduced with permission from ref. 100. Copyright© 2013 American Chemical Society.

 

With the increasing risk and threat to people's health resulting from ongoing use of organophosphorus (OP) compounds, such as pesticides, and potential exposure to chemical nerve agents in terrorist attacks, in military activities, or chemical spills, there is a need to develop new and improved countermeasures and detection schemes for such events. Development of more effective diagnostic technologies for rapid detection of these exposures is essential. There are many methods developed for biomonotoring of exposure to OP agents, such as colorimetric Ellman assay, fluorescence assay, radioactive assay, and the Walter Reed Army Institute of Research (WRAIR) assay.[101] However, these methods need a baseline or a control for an individual in order to detect meaningful changes in blood enzyme levels and are otherwise not accurate. Du *et al.*[101] have developed a simple, rapid, accurate, and reliable detection of exposure to OP agents. This method is based on the magnetic immunodetection for simultaneously measuring enzyme activity and the total amount of enzyme for the diagnosis of OP exposure. The principle of this approach is based on the combination of a MB immunocapture-based enzyme activity assay and a competitive immunoassay for the total amount of enzyme, for simultaneous detection of enzyme inhibition and phosphorylation in biological fluids. Butyrylcholinesterase (BChE) is chosen as a model enzyme (Fig. 19).

Fig. 20 illustrates the principle of combination of enzyme activity assay and immunoassay for detecting OP exposure. Briefly, the sensor detects enzyme activity using magnetic bead (MB)–anti-BChE conjugates to capture BChE in the samples (mixture of OP-inhibited BChE and active BChE) followed by electrochemical detection of electroactive enzymatic products thiocholine (Fig. 20A) based on the following reactions:

$$\mathrm{BTCh} + \mathrm{H_2O} \xrightarrow{\mathrm{BChE}} \text{thiocholine(RSH)} + \mathrm{HA(acetic\ acid)}$$

$$2\text{thiocholine(RSH)} \rightarrow \text{thiocholine(RSSR)} + 2\mathrm{H^+} + 2\mathrm{e^-}$$

As such, enzyme activity measured from samples can be used to calculate active enzyme concentrations according to an established calibration curve of enzyme activity *vs.* enzyme concentration. Here, multi-walled carbon nanotubes (MWNTs) are used to enhance the signal from the oxidation of enzymatic products. Simultaneously, the other sensor can detect total enzyme concentration (mixture of OP-inhibited BChE and active BChE) based on competitive immunoassay using MB–BChE conjugates (Fig. 20B). In this project, MBs conjugated to the BChE and the quantum dots (QDs) served as a label for signal output improvement. The OP-inhibited BChE and active BChE compete with BChE conjugated on the MBs to bind to the limited binding sites of the QD–anti-BChE conjugate in the incubation solution. When the immunoreactions are completed, electrochemical measurements are used to quantify the total amount of BChE by analysis of cadmium ions released from captured quantum dots. Both the total real-time enzyme amount and enzyme activity can be detected in the samples, therefore, we can achieve both enzyme inhibition and the phosphorylation adduct in the samples for detection of exposure to OP agents. This assay shows a linear response over a total BChE concentration range of 0.1–20 nM, and the detection limit is calculated to be as low as 0.05 nM.

### 4.3 Plasma oscillations

The optical transduction by gold nanorods (GNRs) is based upon the phenomenon of localized surface plasmon resonance (LSPR), which arises from the light induced by collective oscillations of surface electrons in the conduction band. The extremely intense and highly localized electro-magnetic fields caused by LSPR make metal NPs highly sensitive to changes in the local refractive index.[102] These changes exhibit a shift of peak wavelength in extinction and scattering spectra proportional to target binding on the nanorod surface. This unique optical property is the basis of their biosensing utility to investigate binding interactions of a variety of biological and pathogenic molecules *via* a label free approach. $Fe_3O_4$ magnetic nanoparticles (MNPs) can greatly enhance the LSPR of metal NPs. The high refractive index and molecular weight of the $Fe_3O_4$ MNPs make them a powerful enhancer for plasmonic responses to biological binding events, thereby enabling a significant improvement in the sensitivity, reliability, dynamic range, and linear calibration of LSPR assays of small molecules in trace amounts. To further evaluate the practical application of $Fe_3O_4$ MNPs in the enhancement of LSPR assays, cardiac troponin I (cTnI)—a protein used for myocardial infarction diagnosis—is used as a model protein to be detected by a GNR bioprobe.

Fig. 21 shows a schematic overview of the MNPs enhanced LSPR assay. Mixing of blood samples and functionalized $Fe_3O_4$ MNPs in the presence of an external magnet results in a specific extraction of cTnI molecules from the physiolofical sample, in the case blood plasma. The MNP amount is excessive as compared to the target

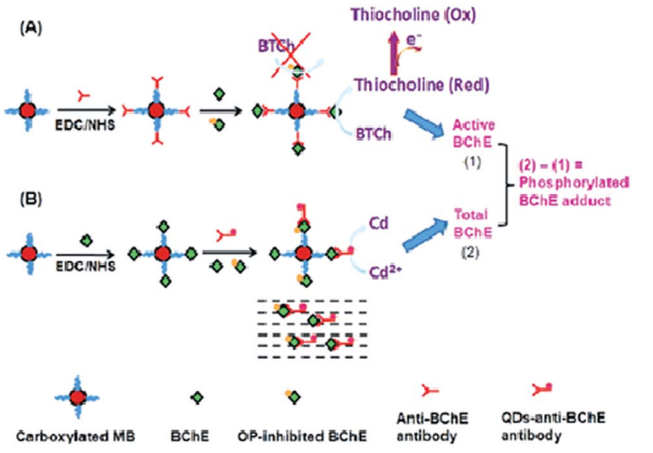


Fig. 20 Schematic illustrations of the principle of immunosensing platform based on (A) immunodetection of enzyme activity and (B) immunoassay of total amount of enzyme simultaneously for biomonitoring of OP exposure. Reproduced with permission from ref. 101. Copyright© 2011 American Chemical Society.

analyte concentration to ensure maximum and efficient cTnI capture. The purified cTnI–MNPs conjugates are then rendered to the LSPR assay using GNR probes. Here, the authors first performed a control study to assess the LSPR shift upon cTnI binding using spiked blood plasma.

The cutoff cTnI value for myocardial infarctions is 0.4–1.0 ng $mL^{-1}$ and can be elevated up to 20 ng $mL^{-1}$, in emergencies—therefore, the target assay range is determined to be 1–20 ng $mL^{-1}$. Fig. 22A shows the calibration curve of the GNR sensor decreased with an increase in the concentration, probably caused by saturation or steric hindrance of the binding sites on the sensor. The LSPR shift for cTnI detection at 1 ng $mL^{-1}$ is about 1 nm. This number is comparable to the background noise of a GNR sensor. Therefore, the detection limit is found to be 5 ng $mL^{-1}$, which is not satisfactory for a clinical diagnosis. Fig. 22B shows a linear relationship between the spectral shift and cTnI concentrations. With the MNP enhancement in spectral sensitivity, defined as relative shift in resonance wavelength with respect to the refractive index change of the surrounding medium, the standard curve is capable of clearly differentiating cTnI amounts in the detection range, thereby allowing extrapolation of cTnI levels in clinical samples for diagnostics.

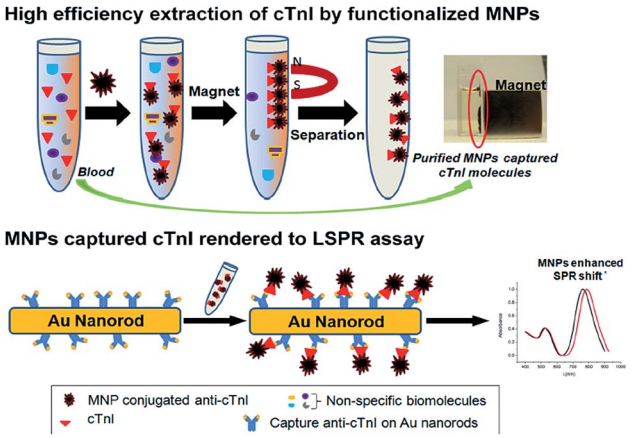


Fig. 21 Schematic showing bioseparation of target molecules from blood plasma by functional $Fe_3O_4$ magnetic nanoparticles (MNPs), followed by the MNP mediated nanoSPR assay. The application of MNP results in an enhancement of the LSPR shift at peak absorption wavelength. Reproduced with permission from ref. 102. Copyright© 2013 American Chemical Society.

## 5. Piezoelectric antibody nanosensors

Piezoelectric (derived from the Greek *piezein* meaning "to press tight, squeeze" and the Greek *elektron* meaning "amber") nanosensors have become increasingly practical and useful tools in biotechnology,[103] clinical diagnostics,[104] structural monitoring,[105] and the food industry[106,107] due to the advantages of cost-effectiveness, experimental simplicity, and real-time output.[108,109] Piezoelectric sensors utilize materials whose crystal structures resonate on the application of an external alternating electrical field. Equally, in these materials, a change in electronic configuration is observable when an external strain acts on the structure. In recent years, quartz crystals (QC) and semiconducting metal

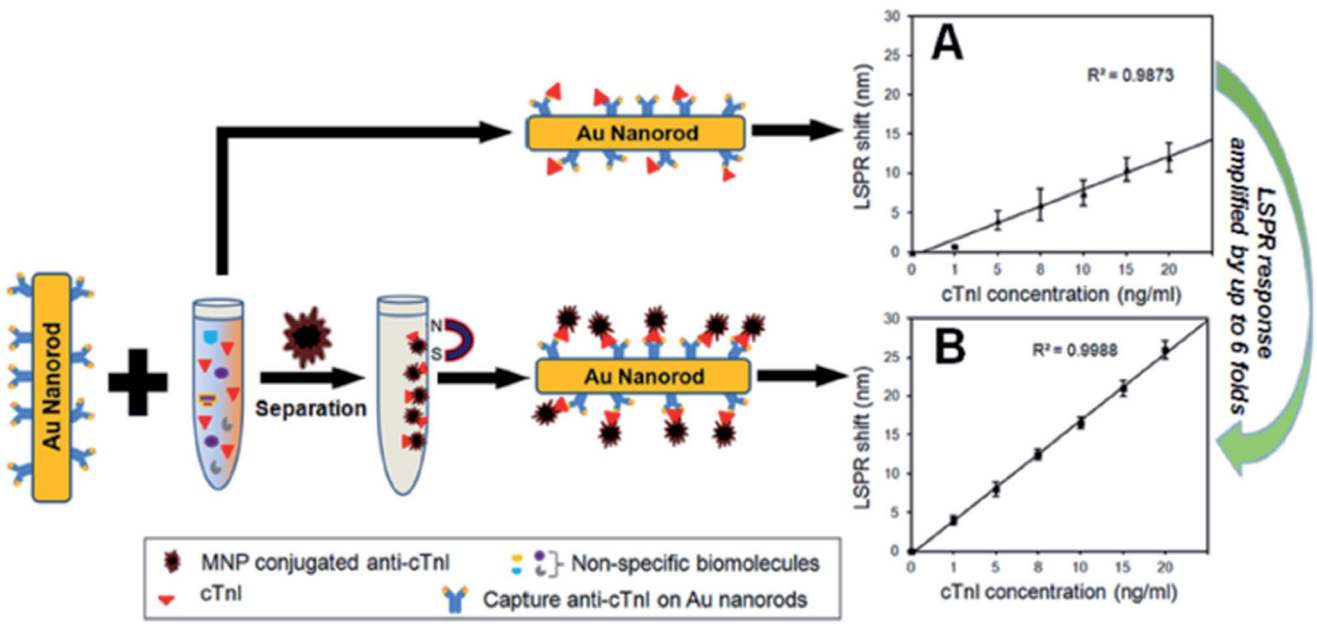


Fig. 22 Effect of the magnetic nanoparticle enhanced LSPR on sensitivity, dynamic range, and reliability of CTnI assay in 40% diluted human blood plasma. (A) Standard curve of LSPR shift as a function of cTnI concentrations without MNPs. (B) Standard curve calibration for MNP enhanced LSPR assay, showing an improved linear relationship between the cTnI concentrations and the LSPR shift resulting from specific binding of $Fe_3O_4$ MNP–cTnI conjugates. The LSPR responses are amplified by up to 6-fold. Reproduced with permission, from Tang *et al.* ref. 102. Copyright© 2013 American Chemical Society.

 

oxide nanowires (NWs) have been confirmed as strong candidates for highly sensitive nanosensors.

### 5.1 Quartz crystals

The transduction of piezoelectric quartz crystal (PQC) nanosensors occurs *via* an oscillating quartz crystal device whose resonance frequency changes with a change in mass, according to the Sauerbrey equation:[110]

$$\Delta F = -2.26 \times 10^{-6} \frac{2F_q^2 \Delta M}{A}$$

where $\Delta F$ is the change in frequency of the crystal, $F_q$ is the fundamental resonant frequency of the crystal, $\Delta M$ is the mass deposited on the electrode surface, and $A$ is the area of the coated crystal. Typical analytes of PQC nanosensors include cells, bacteria, specific proteins, DNA, among many others.[111,112]

Jin *et al.*[113] have realized the analysis of Aflatoxin $B_1$ ($AFB_1$) using PQC sensors by using an indirect competitive immunoassay technique for the detection of the target. The procedure of the probe modification and the later immunoreaction are illustrated in Fig. 23. The developed method is based on a solid phase indirect competitive immunoassay, which is performed as follows. Phosphate buffer solution (PBS) is injected into the reaction cell. Then, analyte containing different concentration of $AFB_1$ is injected into the reaction cell. Subsequently, anti-AFB1 antibody is introduced into the solution, which produces competitive immunoreactions with free $AFB_1$ in solution and is immobilized on the probe surface. Thereafter, a suspension of PBS and gold nanoparticles-labeled goat anti-MIgG antibody is added into the cell. Under determined optimum experimental conditions, the frequency responses of the piezoelectric immunosensor to AFB1 of various concentrations ($C_{AFB1}$) are measured. Fig. 4 shows the frequency change recorded having a statistically significant linear relationship to the $\log(C_{AFB1})$ in the range of 0.1–100 ng $mL^{-1}$, and the correlation coefficient is found to be 0.9962 with a detection limit 0.01 ng $mL^{-1}$ (Fig. 24).

### 5.2 Self-powered piezoelectrics

Recently, semiconducting metal oxide nanowires (NWs), such as ZnO, $SnO_2$, and $In_2O_3$, have been confirmed as strong candidates for highly-sensitive nanosensors due to their high surface-to-volume ratio.[114] In particular, ZnO NWs with applications in biosensing have been intensively investigated because of their biological compatibility and low cost. The biomolecules adsorbed on the surface of ZnO NWs can change the conductance of the NWs by modifying the surface charges and states,[115] disturbing the gate potential,[116] and/or altering the charge-carrier mobility.[117] ZnO NWs with wurtzite crystal structures—a type of hexagonal crystal structure—have attracted international attention due to their high piezoelectric output under externally applied deformation.[118,119] ZnO NW piezoelectric nano-generators (NG) have also been integrated in various self-powered nanosystems.[118] When the *c*-axis of a ZnO NW is under external strain, a piezoelectric field can be induced on the surface that can not only drive the electrons in the external circuit flowing forward and back (the output of NG), but also make the charge-carriers migrate and partially screen this piezoelectric field (*i.e.* – piezotronic effect).[120] If the biosensing and piezo-tronic properties of ZnO NWs can be coupled into a single physical method, new potential for self-powered active nanosensors can be realized through the associated biomolecule-adsorption-dependent piezoelectric output (Fig. 25).

Zhao *et al.*[121] has fabricated new self-powered active nanosensors from ZnO NW piezoelectric NGs with biofunctionalization. The piezoelectric output of the ZnO NW NGs act as both the energy source and biosensing signal. The design and brief fabrication process of the ZnO NGs for self-

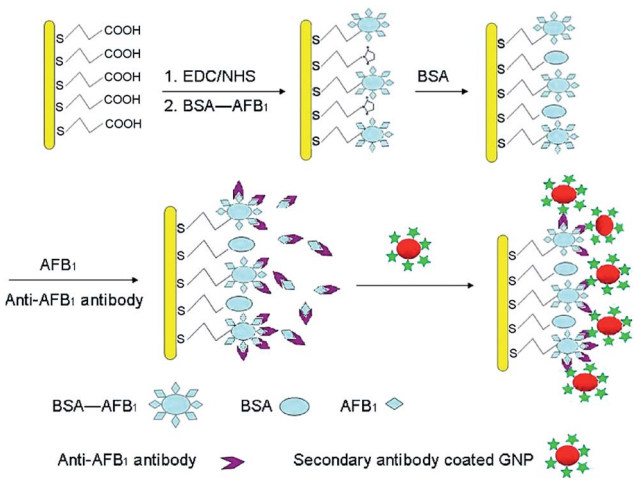


Fig. 23 Schematic illustration of the modification of probe, indirect competitive immunoreaction and the amplification of gold nanoparticles-labeled secondary antibody. Reproduced with permission from ref. 113. Copyright© 2009 Elsevier.

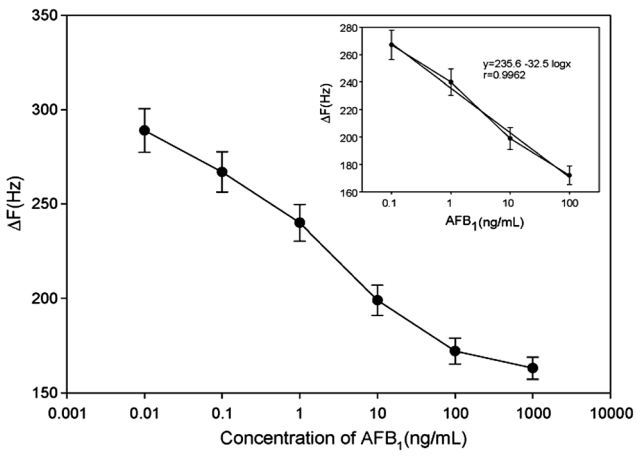


Fig. 24 Calibration curve describing the relationship between the frequency responses and varying concentrations of AFB1 under the optimized conditions, including their linear relationship (inset). The curves are expressed as the frequency decreases against the logarithm of AFB1 concentration. Reproduced with permission from ref. 113. Copyright© 2009 Elsevier.

powered active biosensing is shown in Fig. 5. Firstly, a piece of titanium foil as the substrate of ZnO NW arrays is pre-cleaned (Fig. 5A).

Then vertically-aligned ZnO NW arrays are grown on the titanium substrate by a wet chemical method (Fig. 5B). As shown in Fig. 5C, before detecting IgG, the surface of ZnO NWs needs to be modified with AuNP–anti-IgG by a physical adsorption method. It should be noted that anti-IgG antibody bound AuNPs have been immobilized on the NW surface. A layer of aluminum foil acting as an electrode is placed on ZnO NWs, and two terminal copper leads are glued with silver paste on both electrodes for piezo-electric measurements. After that, the device is tightly fixed between two sheets of flexible Kapton board—a polyimide film used for creating flexible circuits and thermal micrometeoroid garments (space suits)—as the support frame to ensure electric contact between the aluminum foil and the NWs. Fig. 26A shows the room-temperature *I–V* curves of one NG without deformation, showing a typical metal–semiconductor–metal (M–S–M) structure in the device (Al–ZnO–Ti). Compared with the curve of the NG without IgG functionalization, the *I–V* curves shift upwards when the device has been immersed in IgG. As the concentration of IgG increases, the resistance of the device decreases, further confirming that the change of charge-carrier density in ZnO NWs rises from the adsorption of IgG. Under the applied bias voltage of 1.9 V, the current outputs of the device are 0.67470 ± 0140, 0.75770 ± 0047, 0.85470 ± 0099, 0.98170 ± 0154 and 1.06970 ± 0328 mA with the IgG concentrations of 0, $10^{-7}$, $10^{-6}$, $10^{-5}$, and $10^{-4}$ g $mL^{-1}$, respectively, as shown in Fig. 26B (test number $n = 5$). In addition, the RSD ranges from 0.62% to 3.06%. This behavior can be treated as a transistor-type nanosensor (*I–V* behavior). A feasible approach is realized for actively detecting biomolecules by coupling the piezotronic and biosensing characteristics of ZnO NWs.

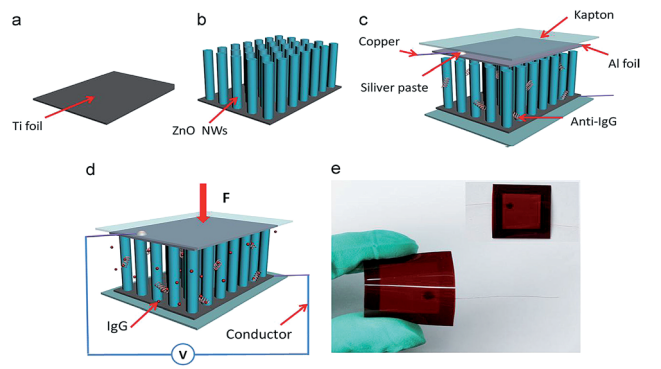


Fig. 25 Fabrication of the self-powered active biosensor. (A) A pre-cleaned Ti foil is used as the substrate. (B) Vertically-aligned ZnO NWs are grown on the Ti foil. (C) The structure design of the self-powered active biosensor after the ant-IgG being assembled onto the surface of ZnO NWs. (D) Schematic image showing the self-powered detecting of IgG. (E) An optical image of the self-powered active biosensor. Reproduced with permission from ref. 121. Copyright© 2014 Elsevier.

## 6. Conclusions: the future of antibody nanosensors

In this review, the authors have discussed novel and prospective antibody nanosensors for the detection of specific analytes from a number of fields of analytical chemistry. Throughout the article, a number of antibody nanosensor transduction methods are reported, including electrochemical, optical, magnetic, and piezoelectric, among others that fall into multiple categories. Table shows the transduction method, antibody, analyte or antigen, lower limit of detection (LLOD), and associated references for key papers discussed within this review. Through this review, it is clear that antibody nanosensors—and nanosensors in general—are highly sensitive no

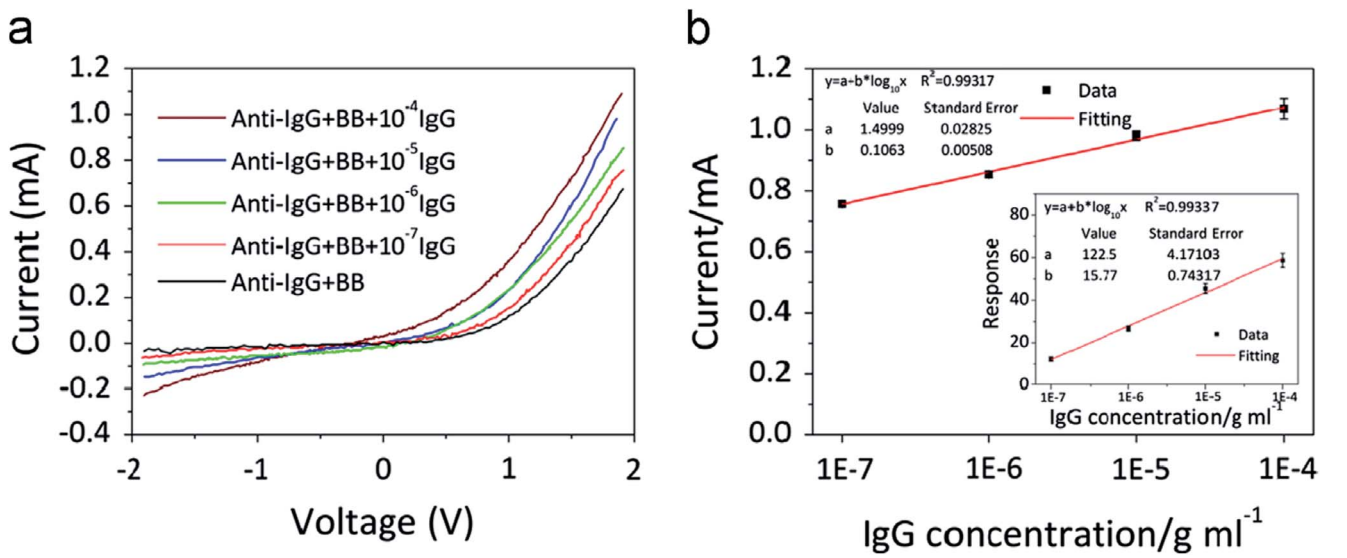


Fig. 26 (A) The *I–V* curves of one device in different concentration of IgG without applied deformation. (B) Current response of the device at a fixed voltage of 1.9 V without applied deformation. The inset shows the response of the device with different concentrations of IgG. Reproduced with permission from ref. 121. Copyright© 2014 Elsevier.

 

matter the transduction method, and that different transduction methods can be suited for a number of different applications.

## Acknowledgements

This work is supported by Texas State Higher Education Assistance Funds (HEAF).

## Notes and references

1 C. Carrillo-Carrión, B. Lendl, B. M. Simonet and M. Valcárcel, *Anal. Chem.*, 2011, **83**, 8093–8100.
2 J. B. Haun, N. K. Devaraj, B. S. Marinelli, H. Lee and R. Weissleder, *ACS Nano*, 2011, **5**, 3204–3213.
3 S. Li and Wiley InterScience, *Biosensor nanomaterials*, Wiley-VCH Verlag, Weinheim, 2011.
4 C. N. Monty, E. K. Wujcik and N. J. Blasdel, Flexible Electrode for Detecting Changes in Temperature, Humidity, and Sodium Ion Concentration in Sweat, *US pat.*, 13/751,199, 28 January 2013.
5 A. A. Volkert and A. J. Haes, *Analyst*, 2014, **139**, 21.
6 E. K. Wujcik, N. J. Blasdel, D. Trowbridge and C. N. Monty, *IEEE Sens. J.*, 2013, **13**, 3430–3436.
7 E. K. Wujcik, N. J. Londoño, S. E. Duirk, C. N. Monty and R. I. Masel, *Chemosphere*, 2013, **91**, 1176–1182.
8 N. Blasdel, E. Wujcik, J. Carletta, K.-S. Lee and C. Monty, *IEEE Sens. J.*, 2014, in press.
9 H. W. Kroto, J. R. Heath, S. C. O'Brien, R. F. Curl and R. E. Smalley, *Nature*, 1985, **318**, 162–163.
10 S. Iijima, *Nature*, 1991, **354**, 56–58.
11 A. K. Geim and K. S. Novoselov, *Nat. Mater.*, 2007, **6**, 183–191.
12 K. S. Novoselov, A. K. Geim, S. V. Morozov, D. Jiang, Y. Zhang, S. V. Dubonos, I. V. Grigorieva and A. A. Firsov, *Science*, 2004, **306**, 666–669.
13 D. Li and Y. Xia, *Adv. Mater.*, 2004, **16**, 1151–1170.
14 Z.-M. Huang, Y.-Z. Zhang, M. Kotaki and S. Ramakrishna, *Compos. Sci. Technol.*, 2003, **63**, 2223–2253.
15 T. Kasuga, M. Hiramatsu, A. Hoson, T. Sekino and K. Niihara, *Adv. Mater.*, 1999, **11**, 1307–1311.
16 Z. L. Wang, R. P. Gao, J. L. Gole and J. D. Stout, *Adv. Mater.*, 2000, **12**, 1938–1940.
17 S. Nie, *Science*, 1997, **275**, 1102–1106.
18 C. A. Mirkin, R. L. Letsinger, R. C. Mucic and J. J. Storhoff, *Nature*, 1996, **382**, 607–609.
19 W. C. Chan, *Science*, 1998, **281**, 2016–2018.
20 I. L. Medintz, H. T. Uyeda, E. R. Goldman and H. Mattoussi, *Nat. Mater.*, 2005, **4**, 435–446.
21 M. A. Correa-Duarte, N. Wagner, J. Rojas-Chapana, C. Morsczeck, M. Thie and M. Giersig, *Nano Lett.*, 2004, **4**, 2233–2236.
22 Z. Liu, C. Davis, W. Cai, L. He, X. Chen and H. Dai, *Proc. Natl. Acad. Sci. U. S. A.*, 2008, **105**, 1410–1415.
23 S. K. Smart, A. I. Cassady, G. Q. Lu and D. J. Martin, *Carbon*, 2006, **44**, 1034–1047.
24 J. Sung, P. W. Barone, H. Kong and M. S. Strano, *Biomaterials*, 2009, **30**, 622–631.
25 E. K. Wujcik and C. N. Monty, *Wiley Interdiscip. Rev.: Nanomed. Nanobiotechnol.*, 2013, **5**, 233–249.
26 A. J. T. George and C. E. Urch, *Diagnostic and therapeutic antibodies*, Humana Press, Totowa, N.J, 2000.
27 W. E. Paul, *Fundamental immunology*, Wolters Kluwer Health/Lippincott Williams & Wilkins, Philadelphia, 2013.
28 V. L. Venkatraman, R. K. Reddy, F. Zhang, D. Evans, B. Ulrich and S. Prasad, *Biosens. Bioelectron.*, 2009, **24**, 3078–3083.
29 K. Gatter, Z. Abdulaziz, P. Beverley, J. Corvalan, C. Ford, E. Lane, M. Mota, J. Nash, K. Pulford, H. Stein, J. Taylor-Papadimitriou, C. Woodhouse and D. Mason, *J. Clin. Pathol.*, 1982, **35**, 1253–1267.
30 F. Ramaekers, C. van Niekerk, L. Poels, E. Schaafsma, A. Huijsmans, H. Robben, G. Schaart and P. Vooijs, *Am. J. Pathol.*, 1990, **136**, 641–655.
31 T. J. Wiktor, A. Flamand and H. Koprowski, *J. Virol. Methods*, 1980, **1**, 33–46.
32 J. A. Kovacs, V. L. Ng, V. L. Ng, G. Leoung, W. K. Hadley, G. Evans, H. C. Lane, F. P. Ognibene, J. Shelhamer, J. E. Parrillo and V. J. Gill, *N. Engl. J. Med.*, 1988, **318**, 589–593.
33 K. Nishimura, *Ann. Intern. Med.*, 2007, **146**, 797.
34 M. B. Lerner, J. Dailey, B. R. Goldsmith, D. Brisson and A. T. Charlie Johnson, *Biosens. Bioelectron.*, 2013, **45**, 163–167.
35 M. Mikulska, T. Calandra, M. Sanguinetti, D. Poulain, C. Viscoli and Third European Conference on Infections in Leukemia Group, *Crit. Care*, 2010, **14**, R222.
36 W. Cha, M. R. Anderson, F. Zhang and M. E. Meyerhoff, *Biosens. Bioelectron.*, 2009, **24**, 2441–2446.
37 E. K. Wujcik, Discovery of Nanostructured Material Properties for Advanced Sensing Platforms, Electronic dissertation, The University of Akron, 2013.
38 E. Baldrich and F. X. Muñoz, *Anal. Chem.*, 2011, **83**, 9244–9250.
39 *Instrumentation and electroanalytical chemistry*, ed. P. R. Unwin, Wiley-VCH, Weinheim, 2003.
40 Q. Huy Tran, A. Tuan Mai, T. Thuy Nguyen, V. Chung Pham and T. Hong Hanh Nguyen, *Adv. Nat. Sci.: Nanosci. Nanotechnol.*, 2012, **3**, 025013.
41 A. Jo, H. Do, G.-J. Jhon, M. Suh and Y. Lee, *Anal. Chem.*, 2011, **83**, 8314–8319.
42 M. Swierczewska, G. Liu, S. Lee and X. Chen, *Chem. Soc. Rev.*, 2012, **41**, 2641.
43 O. A. Sadik, A. O. Aluoch and A. Zhou, *Biosens. Bioelectron.*, 2009, **24**, 2749–2765.
44 D. Tang, H. Li and J. Liao, *Microfluid. Nanofluid.*, 2009, **6**, 403–409.
45 S. K. Yadav, P. Chandra, R. N. Goyal and Y.-B. Shim, *Anal. Chim. Acta*, 2013, **762**, 14–24.
46 S. Guo and E. Wang, *Nano Today*, 2011, **6**, 240–264.
47 N. J. Ronkainen, H. B. Halsall and W. R. Heineman, *Chem. Soc. Rev.*, 2010, **39**, 1747.
48 M. Pohanka and P. Skládal, Electrochemical biosensors – principles and applications, *J. Appl. Biomed.*, 2008, **6**, 57–64.

49 S. Viswanathan and J. Radecki, *Pol. J. Food Nutr. Sci.*, 2008, 58.
50 H. Wei, X. Yan, Q. Wang, S. Wu, Y. Mao, Z. Luo, H. Chen, L. Sun, S. Wei and Z. Guo, *Energy Environ. Focus*, 2013, **2**, 112–120.
51 A. Lupu, P. Lisboa, A. Valsesia, P. Colpo and F. Rossi, *Sens. Actuators, B*, 2009, **137**, 56–61.
52 K. Ding, L. Liu, Y. Cao, X. Yan, H. Wei and Z. Guo, *Int. J. Hydrogen Energy*, 2014, **39**, 7326–7337.
53 J. Guo, H. Gu, H. Wei, Q. Zhang, N. Haldolaarachchige, Y. Li, D. P. Young, S. Wei and Z. Guo, *J. Phys. Chem. C*, 2013, **117**, 10191–10202.
54 W. Suginta, P. Khunkaewla and A. Schulte, *Chem. Rev.*, 2013, **113**, 5458–5479.
55 S. Prasad, A. P. Selvam, R. K. Reddy and A. Love, *J. Lab. Autom.*, 2013, **18**, 143–151.
56 S. Hideshima, R. Sato, S. Inoue, S. Kuroiwa and T. Osaka, *Sens. Actuators, B*, 2012, **161**, 146–150.
57 K.-I. Chen, B.-R. Li and Y.-T. Chen, *Nano Today*, 2011, **6**, 131–154.
58 A. Makaraviciute and A. Ramanaviciene, *Biosens. Bioelectron.*, 2013, **50**, 460–471.
59 R. C. Schmidt and K. E. Healy, *Biomaterials*, 2013, **34**, 3758–3762.
60 H. Gu, J. Guo, X. Yan, H. Wei, X. Zhang, J. Liu, Y. Huang, S. Wei and Z. Guo, *Polymer*, 2014, **55**, 4405–4419.
61 H. Wei, H. Gu, J. Guo, S. Wei, J. Liu and Z. Guo, *J. Phys. Chem. C*, 2013, **117**, 13000–13010.
62 J. Zhu, M. Chen, H. Qu, X. Zhang, H. Wei, Z. Luo, H. A. Colorado, S. Wei and Z. Guo, *Polymer*, 2012, **53**, 5953–5964.
63 S. Cosnier and M. Holzinger, *Chem. Soc. Rev.*, 2011, **40**, 2146.
64 C. Dhand, M. Das, M. Datta and B. D. Malhotra, *Biosens. Bioelectron.*, 2011, **26**, 2811–2821.
65 M. Perfézou, A. Turner and A. Merkoçi, *Chem. Soc. Rev.*, 2012, **41**, 2606.
66 H. Gu, X. Zhang, H. Wei, Y. Huang, S. Wei and Z. Guo, *Chem. Soc. Rev.*, 2013, **42**, 5907.
67 H. Wang, Z. Xu, H. Yi, H. Wei, Z. Guo and X. Wang, *Nano Energy*, 2014, **7**, 86–96.
68 H. Wei, H. Gu, J. Guo, S. Wei and Z. Guo, *ECS J. Solid State Sci. Technol.*, 2013, **2**, M3008–M3014.
69 H. Wei, X. Yan, Y. Li, S. Wu, A. Wang, S. Wei and Z. Guo, *J. Phys. Chem. C*, 2012, **116**, 4500–4510.
70 K. Ding, Y. Wang, H. Yang, C. Zheng, Y. Cao, H. Wei, Y. Wang and Z. Guo, *Electrochim. Acta*, 2013, **100**, 147–156.
71 L. Saghatforoush, M. Hasanzadeh and N. Shadjou, *Chin. Chem. Lett.*, 2014, **25**, 655–658.
72 N. Sanvicens, C. Pastells, N. Pascual and M.-P. Marco, *TrAC, Trends Anal. Chem.*, 2009, **28**, 1243–1252.
73 D. Grieshaber, R. MacKenzie, J. Vörös and E. Reimhult, *Sensors*, 2008, **8**, 1400–1458.
74 J. F. Rusling, C. V. Kumar, J. S. Gutkind and V. Patel, *Analyst*, 2010, **135**, 2496.
75 B. Jin, P. Wang, H. Mao, B. Hu, H. Zhang, Z. Cheng, Z. Wu, X. Bian, C. Jia, F. Jing, Q. Jin and J. Zhao, *Biosens. Bioelectron.*, 2014, **55**, 464–469.
76 W. Siangproh, W. Dungchai, P. Rattanarat and O. Chailapakul, *Anal. Chim. Acta*, 2011, **690**, 10–25.
77 A. Erdem, K. Kerman, B. Meric, U. S. Akarca and M. Ozsoz, *Anal. Chim. Acta*, 2000, **422**, 139–149.
78 B. Zhang, B. Liu, J. Liao, G. Chen and D. Tang, *Anal. Chem.*, 2013, **85**, 9245–9252.
79 E. Suprun, T. Bulko, A. Lisitsa, O. Gnedenko, A. Ivanov, V. Shumyantseva and A. Archakov, *Biosens. Bioelectron.*, 2010, **25**, 1694–1698.
80 Y.-T. Chang, J.-H. Huang, M.-C. Tu, P. Chang and T.-R. Yew, *Biosens. Bioelectron.*, 2013, **41**, 898–902.
81 C. Hu, D.-P. Yang, K. Xu, H. Cao, B. Wu, D. Cui and N. Jia, *Anal. Chem.*, 2012, **84**, 10324–10331.
82 B. B. Kim, W. J. Im, J. Y. Byun, H. M. Kim, M.-G. Kim and Y.-B. Shin, *Sens. Actuators, B*, 2014, **190**, 243–248.
83 G. Wandermur, D. Rodrigues, R. Allil, V. Queiroz, R. Peixoto, M. Werneck and M. Miguel, *Biosens. Bioelectron.*, 2014, **54**, 661–666.
84 J. Tian, L. Zhou, Y. Zhao, Y. Wang, Y. Peng and S. Zhao, *Talanta*, 2012, **92**, 72–77.
85 H. M. Hiep, H. Yoshikawa and E. Tamiya, *Anal. Chem.*, 2010, **82**, 1221–1227.
86 W. P. Hall, S. N. Ngatia and R. P. Van Duyne, *J. Phys. Chem. C*, 2011, **115**, 1410–1414.
87 M.-P. Marco, S. Gee and B. D. Hammock, *TrAC, Trends Anal. Chem.*, 1995, **14**, 341–350.
88 R. de la Rica and M. M. Stevens, *Nat. Nanotechnol.*, 2012, **7**, 821–824.
89 S. Lai, S. Wang, J. Luo, L. J. Lee, S.-T. Yang and M. J. Madou, *Anal. Chem.*, 2004, **76**, 1832–1837.
90 S. Chen, M. Svedendahl, R. P. V. Duyne and M. Käll, *Nano Lett.*, 2011, **11**, 1826–1830.
91 S.-W. Lee, K.-S. Lee, J. Ahn, J.-J. Lee, M.-G. Kim and Y.-B. Shin, *ACS Nano*, 2011, **5**, 897–904.
92 L. Rodríguez-Lorenzo, R. de la Rica, R. A. Álvarez-Puebla, L. M. Liz-Marzán and M. M. Stevens, *Nat. Mater.*, 2012, **11**, 604–607.
93 D. M. Rissin, C. W. Kan, T. G. Campbell, S. C. Howes, D. R. Fournier, L. Song, T. Piech, P. P. Patel, L. Chang, A. J. Rivnak, E. P. Ferrell, J. D. Randall, G. K. Provuncher, D. R. Walt and D. C. Duffy, *Nat. Biotechnol.*, 2010, **28**, 595–599.
94 H. Huang, S. Huang, X. Liu, Y. Zeng, X. Yu, B. Liao and Y. Chen, *Biosens. Bioelectron.*, 2009, **24**, 3025–3029.
95 M. Colombo, S. Ronchi, D. Monti, F. Corsi, E. Trabucchi and D. Prosperi, *Anal. Biochem.*, 2009, **392**, 96–102.
96 H. Gu, J. Guo, H. Wei, X. Zhang, J. Zhu, L. Shao, Y. Huang, N. Haldolaarachchige, D. P. Young, S. Wei and Z. Guo, *Polymer*, 2014, **55**, 944–950.
97 H. Gu, Y. Huang, X. Zhang, Q. Wang, J. Zhu, L. Shao, N. Haldolaarachchige, D. P. Young, S. Wei and Z. Guo, *Polymer*, 2012, **53**, 801–809.
98 J. Zhu, H. Gu, Z. Luo, N. Haldolaarachige, D. P. Young, S. Wei and Z. Guo, *Langmuir*, 2012, **28**, 10246–10255.
99 D. Kim, F. Marchetti, Z. Chen, S. Zaric, R. J. Wilson, D. A. Hall, R. S. Gaster, J.-R. Lee, J. Wang, S. J. Osterfeld, H. Yu, R. M. White, W. F. Blakely, L. E. Peterson,

 

S. Bhatnagar, B. Mannion, S. Tseng, K. Roth, M. Coleman, A. M. Snijders, A. J. Wyrobek and S. X. Wang, *Sci. Rep.*, 2013, **3**, 2234.
100 Z. Gao, M. Xu, L. Hou, G. Chen and D. Tang, *Anal. Chem.*, 2013, **85**, 6945–6952.
101 D. Du, J. Wang, L. Wang, D. Lu, J. N. Smith, C. Timchalk and Y. Lin, *Anal. Chem.*, 2011, **83**, 3770–3777.
102 L. Tang, J. Casas and M. Venkataramasubramani, *Anal. Chem.*, 2013, **85**, 1431–1439.
103 C. R. Suri, M. Raje and G. C. Mishra, *Biosens. Bioelectron.*, 1994, **9**, 325–332.
104 B. D. Malhotra and A. Chaubey, *Sens. Actuators, B*, 2003, **91**, 117–127.
105 X. Zhao, T. Qian, G. Mei, C. Kwan, R. Zane, C. Walsh, T. Paing and Z. Popovic, *Smart Mater. Struct.*, 2007, **16**, 1218–1225.
106 X. Guo, C.-S. Lin, S.-H. Chen, R. Ye and V. C. H. Wu, *Biosens. Bioelectron.*, 2012, **38**, 177–183.
107 M. Taniwaki, T. Hanada and N. Sakurai, *Food Res. Int.*, 2006, **39**, 1099–1105.
108 R. L. Bunde, E. J. Jarvi and J. J. Rosentreter, *Talanta*, 1998, **46**, 1223–1236.
109 A. Janshoff, H.-J. Galla and C. Steinem, *Angew. Chem.*, 2000, **39**, 4004–4032.
110 G. Sauerbrey, *Z. Phys.*, 1959, **155**, 206–222.
111 Y. S. Fung and Y. Y. Wong, *Anal. Chem.*, 2001, **73**, 5302–5309.
112 X. Su, R. Robelek, Y. Wu, G. Wang and W. Knoll, *Anal. Chem.*, 2004, **76**, 489–494.
113 X. Jin, X. Jin, L. Chen, J. Jiang, G. Shen and R. Yu, *Biosens. Bioelectron.*, 2009, **24**, 2580–2585.
114 P.-H. Yeh, Z. Li and Z. L. Wang, *Adv. Mater.*, 2009, **21**, 4975–4978.
115 Y. Cui, Q. Wei, H. Park and C. M. Lieber, *Science*, 2001, **293**, 1289–1292.
116 J. H. He, Y. Y. Zhang, J. Liu, D. Moore, G. Bao and Z. L. Wang, *J. Phys. Chem. C*, 2007, **111**, 12152–12156.
117 A. Maroto, K. Balasubramanian, M. Burghard and K. Kern, *ChemPhysChem*, 2007, **8**, 220–223.
118 Z. L. Wang, *Science*, 2006, **312**, 242–246.
119 S. Xu, Y. Qin, C. Xu, Y. Wei, R. Yang and Z. L. Wang, *Nat. Nanotechnol.*, 2010, **5**, 366–373.
120 C. Pan, Z. Li, W. Guo, J. Zhu and Z. L. Wang, *Angew. Chem.*, 2011, **123**, 11388–11392.
121 Y. Zhao, P. Deng, Y. Nie, P. Wang, Y. Zhang, L. Xing and X. Xue, *Biosens. Bioelectron.*, 2014, **57**, 269–275.
122 S.-W. Lee, K.-S. Lee, J. Ahn, J.-J. Lee, M.-G. Kim and Y.-B. Shin, *ACS Nano*, 2011, **5**, 897–904.